



Invited review

The Earth's coda correlation wavefield: Rise of the new paradigm and recent advances



Hrvoje Tkalčić*, Thanh-Son Phạm, Sheng Wang

Research School of Earth Sciences, The Australian National University, 142 Mills Road, Canberra, ACT 2601, Australia

ARTICLE INFO

Keywords:
 Correlation wavefield
 Cross-correlation
 Coda correlation
 Seismic wavefield
 Global seismology
 Deep Earth studies
 Earth's inner core
 Data processing
 Codacorrelation tomography

ABSTRACT

Seismology has come a long way in providing insights into Earth's internal structure and dynamics. Among many forward and inverse geophysical techniques developed, full waveform modelling, seismic tomography and receiver-based studies enabled detailed imaging of Earth's subsurface. The invention of ambient noise tomography within the last two decades revolutionized studies of Earth's subsurface based on the cross-correlation of the Earth's ambient noise. That method, in particular, enabled imaging of Earth structure in places where earthquakes or receivers do not exist. At the same time, progress in imaging the Earth's deepest shells has been impeded by the lack of geometric coverage of body waves due to uneven global distribution of seismic sources and receivers and the fact that the ambient noise studies cannot reach deeper than the uppermost Earth's shells, near its surface. In seeking the ways forward, global seismologists started experimenting with cross-correlating the part of the seismograms recorded many hours after the first arrivals of body-waves, the so-called earthquake coda. As in many science disciplines, initial work on this topic resulted in controversies but also led to new realisations and discoveries that all contributed to the rise of a new paradigm – the earthquake coda-correlation wavefield, which is the focus of this review paper. We do not attempt here to provide a review of ambient-noise correlation, although we use some familiar concepts to introduce coda-correlation. Our main goal is to review theoretical and observational work to date that resulted in a better understanding of the coda-correlation wavefield, both as a phenomenon and a powerful method. The features in global correlograms exist due to many cross-terms of reverberating body-waves, a principle fundamentally different from the reconstruction of surface waves in the ambient-noise correlograms. Once the coda-correlation wavefield is fully understood through theoretical developments, the method becomes a powerful way to study Earth's deep structure. Apart from providing a review of the most important results to date, we scrutinise the process of making global correlograms and analyse their characteristics while taking into consideration various aspects, such as the time after the earthquake, the source-receiver geometries, the level of seismicity and the type of earthquake mechanism. Furthermore, we provide practical examples on how to build correlograms and interpret correlogram features using programming language Python. Our review seeks to promote the topic of coda correlation among already experienced researchers as well as students who embark on this interesting research, which may play a central role in global and planetary seismology in the coming decades.

1. Introduction

The earthquake-coda correlation-wavefield emerged in the last several years not only as a new concept, but also as a potentially powerful new technique that could be applied to address a number of open questions in global seismology. These questions are revolving around the existing uncertainties on Earth structure, especially those pertaining to the Earth's deep interior and near the main structural-boundaries in spherically-symmetric Earth models. On a more general level, the open questions extend to the 3D structure of the entire Earth,

and other terrestrial planets. At this stage of theoretical and application developments, we are exploring avenues for complementing the existing seismic wavefield techniques and filling the gaps in our knowledge due to the lack of seismic data and uneven sampling of the Earth's interior.

This review manuscript first presents the theory (Section 2), which is then followed by the methods/techniques section (Section 3). The theory section is presented in a way that it follows the chronology of relevant literature, whereas the methods section builds on and expands further some of the ideas explored in the theory section. Finally, the

* Corresponding author.

E-mail address: Hrvoje.Tkalcic@anu.edu.au (H. Tkalčić).

applications (Section 4) discusses some of the research directions, most notably the studies of the Earth's core and coda-correlation tomography.

Instead of perusing figures from previous publications, we revisit and expand some key experiments for the purposes of this review paper. We hope that it will serve not just as a starting point for researchers who begin to explore the correlation wavefield, but also as a good reference for those who are already experienced users. Last but not least, we provide Python examples for some of the key procedures, which we hope will find the use in future endeavours.

2. Theoretical background

2.1. Cross-correlations in ambient noise wavefield and surface-wave reconstructions

In the discipline of seismology, a cross-correlation function is often utilised as a measure of similarity between two ground-motion time series, also known as seismograms. It is not difficult to see why this measure would be useful when comparing the observed and synthetic seismograms or studying the waveforms of repeating earthquakes. Another important application of cross-correlation at the global scale can be traced back to the studies of the so-called “ambient-noise” field. The ambient-noise is present due to constant interaction among the solid Earth, atmosphere and oceans, but also due to natural seismicity and human activities (e.g., transportations or building constructions) and the seismic wavefield interactions with subsurface scatterers and discontinuities (e.g., Bonnefoy-Claudet et al., 2006; Kobayashi and Nishida, 1998; Nishida et al., 2002; Rhie and Romanowicz, 2004).

It has been theoretically shown that the cross-correlation between continuous recordings of a completely diffuse wavefield at two seismic receivers equals the inter-receiver medium response (Green's functions) convolved by the stacked auto-correlation of noise source-time functions. In other words, according to this principle, it is possible to construct a seismic response through cross-correlating seismograms at places where earthquakes do not occur. This principle was initially conjectured for 1D media by Claerbout (1968), who derived the acoustic reflection response of a layered media via autocorrelation techniques. The principle is generalised for elastic wave propagation in 3D media, and accessible proofs were derived in a number of past review papers (e.g., Boschi and Weemstra, 2015; Galetti and Curtis, 2012; Snieder and Larose, 2013; Wapenaar et al., 2010). In mathematical terms, this relationship can be expressed by:

$$[G(x_B, x_A; t) + G(x_B, x_A; -t)] * S_N(t) = f_A(t) * f_B(-t) = f_A(t) \star f_B(t), \quad (1)$$

where $f_A(t)$ and $f_B(t)$ are the recordings at the receivers x_A and x_B , respectively, $*$ and \star denote the convolution and correlation operators, $G(x_B, x_A; t)$ is the Green's function between the receivers x_A and x_B , $G(x_B, x_A, -t)$ represents its time-reversal, and $S_N(t)$ is the stacked auto-correlation of the source-time function over numerous noise sources.

In simple terms, the above principle enables the use of continuous waveform cross-correlation to reconstruct the medium response as if ground motion is measured at one of the receivers from a virtual source located at the other. Pioneering studies demonstrated that the surface-wave structural responses between receiver pairs can be obtained routinely by cross-correlating the ambient noise records because in certain circumstances, the ambient field is a good approximation of a diffuse wavefield (Campillo and Paul, 2003; Shapiro and Campillo, 2004; Shapiro et al., 2005). Subsequently, this method revolutionized the imaging techniques (e.g., Bensen et al., 2008; Lin et al., 2007, 2008; Moschetti et al., 2007; Yao et al., 2006) and passive monitoring of temporal changes (e.g., Brenguier et al., 2008; Yates et al., 2019) of shallow Earth structures in many regions in the last two decades. Thus, the term “Green's function retrieval” or “Green's function reconstruction” was gradually accepted.

Cross-correlation, however, does not necessarily yield the Green's function unless the wavefield that is cross-correlated is a diffuse wavefield. This is theoretically demonstrated by Snieder (2004) and Wapenaar et al. (2010). A diffuse wavefield is a field in which wave energy can be described by equal intensity distribution in different directions, and wave amplitude is comparable in any time and spatial domain. Weaver and Lobkis (2004, 2006) studied details of a diffuse wavefield. The level of diffuseness of a wavefield determines the goodness of the Green's function retrieval. That being said, Wapenaar and Fokkema (2006) noted the striking resemblance with the retrieval of Green's tensor in diffuse wavefields such as the ambient noise wavefield on the Earth's free surface (Campillo and Paul, 2003; Shapiro and Campillo, 2004).

In order to illustrate the dependency of the Green's function retrieval on the diffuseness of a wavefield, we revisited the experiments of Wapenaar et al. (2010) and Fichtner (2014). In our experiment (Fig. 1), the medium is homogeneous, with waves propagating across the surface at a constant velocity of 3000 m/s. The ambient noise is represented by many simultaneous point sources (black dots) with random noise time series in the frequency range 1.0–25.0 Hz, and the duration of the noise series is 10,000 s. The two receivers (red triangles) are located at the coordinates (6000 m, 0 m) and (-6000 m, 0 m), so that the propagation time between them is 4 s. We set two types of source event distributions: one type presents isotropic (uniform) source distribution in different directions (Fig. 1A and C), and the other type presents heterogeneous sources (Fig. 1D–I). The former yields equally-distributed wave-incidences from all directions, whereas the latter shows limited range of wave incidences. The cross-correlations of these two types of wavefields show a significant difference: the former (Fig. 1A and C) has two clear spikes, at -4 s and 4 s. The spike at 4 s corresponds to the Green's function resembling the propagation from the right to the left receiver, and the spike at -4 s corresponds to the Green's function resembling the propagation from the left to the right receiver (see Eq. (1)). In contrast, the spike at -4 s does not exist (Fig. 1D and E) when the sources are absent on the left side. For some source distributions, neither spikes at 4 s nor at -4 s exist, and there are cross-correlation signals that do not correspond to the response between the two receivers (Figs. 1F–I).

A diffuse field can be approximately created by many uncorrelated and equally-distributed sources from the perspective of a receiver pair (Snieder, 2004; Wapenaar, 2004; Wapenaar et al., 2010; Weaver and Lobkis, 2001). The sources can be seismic events or secondary sources due to heterogeneity (inhomogeneity) of the medium and the existence of scatterers. In the real world, continuous seismic recording consists of waves from both the primary and secondary sources that occur simultaneously.

The diffuseness of a seismic wavefield is significantly modified by the existence of heterogeneity and attenuation in Earth's interior. Structural heterogeneity alters the wavefield propagation through reflection, refraction and diffraction, and increases the equity of energy distribution: widespread scatterers act as secondary sources and hence increase the diffuseness. The attenuation effect may decrease the diffuseness. For example, waves from a relatively small seismic event are fully attenuated after propagating for a few kilometres, and that can determine the wave-energy incidence from a specific direction. If the medium is perfectly lossless, i.e. free of attenuation effects, the wavefield propagation after a certain period of time would be fully determined by structure randomness, however that condition is not satisfied in real Earth. Fan and Snieder (2009) and Wapenaar et al. (2010) warned that inter-receiver cross-correlation function could be different from the Green's function even if the medium is fully illuminated by wave energy due to many scatterers.

Snieder (2004) and Wapenaar and Fokkema (2006) showed that the requirement for equally-distributed sources can be relaxed to fewer sources that are located near the stationary points of the two seismic arrivals, which are defined as point source locations with nearly

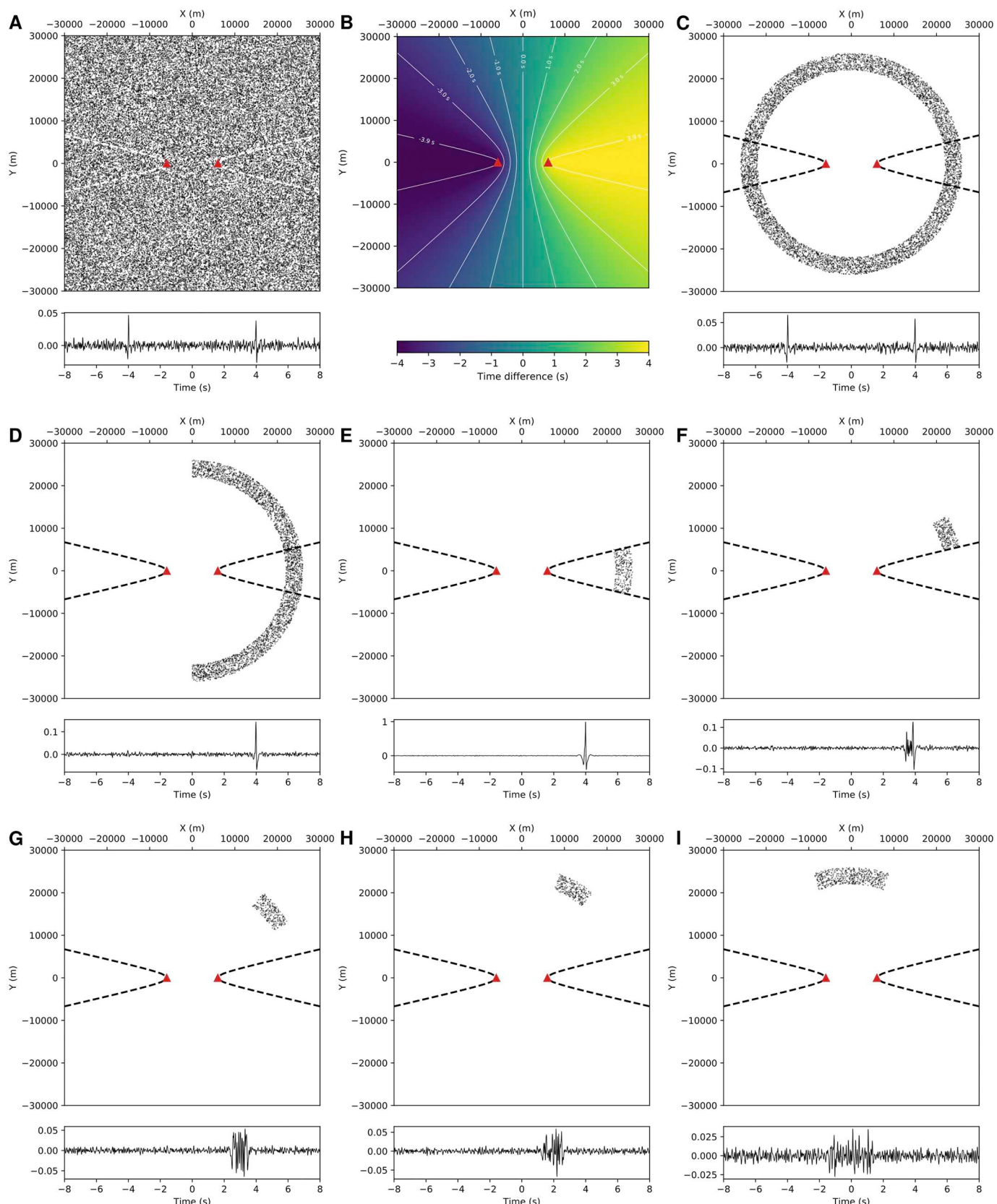


Fig. 1. Illustration of the cross-correlation principle in 2D and the concept of Fresnel zones for a homogenous medium and the seismic velocity in the medium equal to 3000 m/s. Simultaneously acting noise sources are used with random source-time-function in the range 1.0–25.0 Hz, and the duration of the noise series is 10,000 s. (A) Uniformly distributed noise sources (black points) around two receivers (red triangles), and inter-receiver cross-correlation of continuous recordings corresponding to the wavefield. The traveltimes from one receiver to the other is 4.0 s. The Fresnel zone is shown by dashed lines. See the text for the definition of the Fresnel zone. (B) Contour of the differential traveltimes between two seismic waves emanated from different point-source locations to the two receivers. Contour lines present the time difference of -3.9 s , -3.0 s , -2.0 s , -1.0 s , 0.0 s , 1.0 s , 2.0 s , 3.0 s , 3.9 s . (C) Same as (A) but with a finite-width ring of noise sources. (D–J) Same as (C), but for azimuthally-varying distributions of noise sources in the counter-clockwise direction. Note the variation in the amplitude scale of the cross-correlation function.

invariant (i.e., the first derivative vanishes) of differential travel time to the receivers. For a specific example shown in Fig. 1, when the medium is homogeneous, the stationary points are on the line passing through the two receivers. The derivations employing stationary-phase approximation demonstrate that the recorded waves from a source far away from that line are uncorrelated, and the reconstruction of surface waves is favoured by the sources along the line because the recorded waves interfere constructively in the cross-correlation. Considering the finiteness of the frequencies involved, a finite-size area around the line passing through the two receivers – a.k.a. the Fresnel zone, can be determined. The sources inside the Fresnel zone constructively contribute to the surface-wave features in the cross-correlation, whereas the contributions from the sources outside the Fresnel zone interfere destructively.

In Fig. 1, we qualitatively choose a finite-size Fresnel zone around the line passing through the two given receivers based on the time difference for the waves arriving from a given point source to these two receivers (Fig. 1B). For any source inside the Fresnel zone, the time difference between two seismic waves recorded at the two receivers is within 0.1 s compared to the seismic-wave traveltimes between the two receivers (4 s), that is, the absolute time difference is larger than 3.9 s. Outside the Fresnel zone, that time difference is larger than 0.1 s, that is, the absolute time difference is smaller than 3.9 s. Expressed more quantitatively, 0.1 s corresponds to 1/10 of the longest period used in the experiment. The sources inside the Fresnel zone effectively reconstruct the seismic waves at 4 s (Fig. 1E), whereas the sources outside the Fresnel zone fail to produce a spike at 4 s and there are cross-correlation features that do not correspond to the reconstructed seismic wave (Fig. 1F–I).

Furthermore, inside the Fresnel zone the time difference from a given point source to the two receivers is nearly invariant to source locations, and outside the Fresnel zone that time difference presents considerable azimuthal, but no variations in radius. This provides an intuitive explanation for why a ring distribution (Fig. 1C) is equivalent to a uniform distribution of sources (Fig. 1A). We will revisit the variations of the time difference due to different source-locations later, and we will use the first-order derivatives with respect to the source locations.

The Fresnel zone analysis is important to distinguish between constructive and destructive contributions and to determine accuracy of the wave reconstruction. Sager et al. (2018) show that a Fresnel zone is stable and wide on the Earth's free surface for surface wave reconstruction. That can be simply derived through treating the surface wave ray-paths as great-circle paths on a spherical surface between the two receivers because surface-wave's wavelengths are around tens to a few hundred kilometres given the surface-wave finite-frequency band around few mHz and their velocity around several kilometres per second. Apart from that, both receivers and sources, the latter either due to the interaction of atmosphere and ocean with the solid earth or due to anthropogenic activities, are either on or near the Earth's free surface. Therefore, surface waves that propagate along the two-dimensional Earth's free surface can be stably reconstructed from cross-correlations in ambient-noise field. The “Green's function retrieval” or “surface-waves reconstruction” achieved a significant success since the pioneering works of Campillo and Paul (2003) and Shapiro et al. (2005). This led to numerous studies that used the reconstructed surface waves from ambient noise wavefield to infer the underground structure (F.-C. Lin et al., 2008, e.g., Lin et al., 2007; Yang et al., 2007; Yao et al., 2006; Zheng et al., 2008).

2.2. Reconstruction of body-waves in global coda-correlation under scrutiny

We have so far seen how the equivalence of surface-wave propagation can be reconstructed for a pair of receivers on Earth's surface, but what about body waves? It has become a usual practice to form stacks of cross-correlation functions with inter-receiver distance

(correlograms) of both the ambient noise and the seismic-event coda wavefields (Fig. 2a). Apart from the retrieval of surface waves, many features that resemble body-wave phases in the direct wavefield were observed in those stacks for both regional (e.g., Poli et al., 2012a, 2012b; Zhan et al., 2010) and global scales (Boué et al., 2014, e.g., Boué et al., 2013; Lin et al., 2013; Lin and Tsai, 2013; Nishida, 2013; Xia et al., 2016).

However, the accurate “body-wave reconstruction” requires seismic sources, which can be either primary or secondary, to be concentrated near the stationary points. Wapenaar et al. (2010) showed the configuration for local body-wave reconstruction, and Ruigrok et al. (2008) illustrated the settings for the global phase-reconstructions. In general, this requirement is difficult to fulfil for body-wave settings as previously discussed in (Forghani and Snieder, 2010). Indeed, there do not exist many densely distributed sources within Earth's interior that would favour body-wave reconstruction as is the case for surface-wave reconstruction near its surface (although this is also somewhat true for the noise generated by atmosphere-ocean-solid earth interactions). Most of earthquakes are confined to the upper and middle crust, and almost all of human-activity-related sources are within few hundred meters from the free surface. Even though there are, occasionally, considerably deep events, the existence of relatively strong attenuation at shallow depths would significantly depress equally-distributed wave energy.

Therefore, in the ambient noise regime, the most plausible conclusion was that the observation of body-wave-related features in correlograms depended on specific conditions of the study region. For example, Zhan et al. (2010) analysed cross-correlation features that are related to the Moho reflections in the Kaapvaal craton, South Africa. In that area, sufficient seismic energy is trapped within the crust due to the sharp contrast between the crust and mantle velocities. A similar result was obtained in a study of the Karoo region in RSA from active seismic lines (Ryberg, 2011). Snieder (2004) demonstrated that a sharp Moho, or other subsurface discontinuities, perform as “mirrors” to create virtual sources at depth that are images of the sources concentrated near the Earth's free surface. Also, apart from strong scattering in the crust in a relatively short-period band (1–5 s), there are topography effects that increase the diffuseness of the ambient-noise wavefield. In other words, they make a proxy for a distribution of many sources in a three-dimensional crustal volume and produce a quasi-uniform distribution of energy that allows for body-wave reconstructions. It could be that for the same reasons, Poli et al., 2012a observed P and S waves reflected from Moho in the northern part of the Fennoscandian region, and Pedersen and Colombi (2018) observed body-wave reflections related to the upper-mantle discontinuities.

A more convenient way to achieve the steep illumination is to employ the recordings of teleseismic earthquakes, where the local stratified structures are illuminated from steep-arriving teleseismic waves. Claerbout (1968) and Scherbaum (1987) proved that the auto-correlation of vertical transmission response in a layered model converges to the vertical reflection response. Characterized by vertical energy incidence, recordings of teleseismic earthquakes have proved to be more efficient in extracting reflections under a receiver site (e.g., Phạm and Tkalčić, 2017, 2018; Ruigrok and Wapenaar, 2012; Sun and Kennett, 2016; Tauzin et al., 2019).

On the global scale, the features that resemble body waves are observed after applying the same cross-correlation and stacking techniques to continuous recordings for receiver pairs separated by teleseismic distances. Poli et al., 2012b first identified P waves reflected by the upper-mantle discontinuities and used these observations to infer the properties of the mantle-transition zone. Lin and Tsai (2013) reported that hourly cross-correlation stacks (correlograms) at antipodal inter-receiver distances yielded prominent features that were similar to body waves in the seismic wavefield. These features are stable and coherent both for regional seismic arrays (Lin et al., 2013; Poli et al., 2015) and for global networks (Boué et al., 2013, 2014; Nishida, 2013).

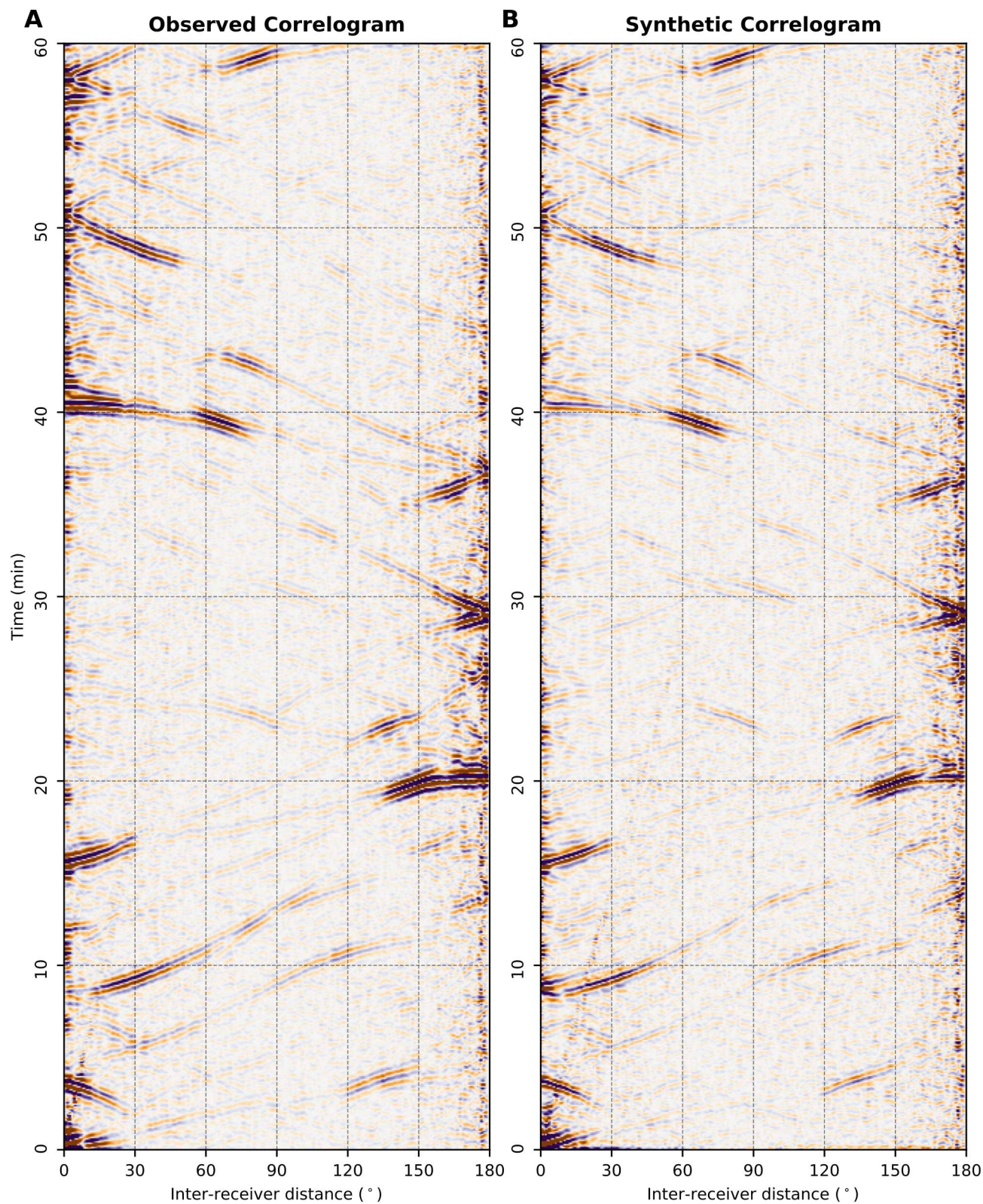


Fig. 2. The Earth's correlation wavefield. (A) Observed and (B) synthetic cross correlograms for the binned interstation distance with the bin size of 1° (see the Methods section). Cross correlograms are prefiltered in the period band of 15–50 s. Red and blue colours show the positive and negative amplitudes. (For interpretation of the references to color in this figure legend, the reader is referred to the web version of this article.)

They were initially thought to be part of the Green's function accurately reconstructed from a diffusive wavefield at the global scale as in the case of surface waves emerging from ambient noise.

It was then shown that prominent features in global correlograms

were related to large earthquakes (see Section 3.3). Lin et al. (2013) and Boué et al. (2014) distinguished between global correlograms for “active” and “quiet” days with respect to global seismicity and suggested a strong causal relationship between the correlation features and large

earthquakes. An equal distribution of energy is the primary probe to the diffuseness of a wavefield. [Sens-Schönenfelder et al. \(2015\)](#) measured the energy distribution of late coda and demonstrated that the earthquake-coda is dominated by steep reverberation along the great circle path to the recording array. The coda field is far from a diffuse wavefield that is a prerequisite for an accurate reconstruction of body wave Green's function between two receivers (see [Section 3.3.5.](#)).

Consequently, there were concerns on the reliability of the Green's function theory (i.e. that the same set of assumptions and theory that is applied to surface waves can be valid for body waves) among the global interferometry community ([Boué et al., 2014](#)). In the next section, we review the recent advancements in the understanding of the formation of global correlograms.

2.3. Formation of global coda-correlation features

Apart from the arguments that the seismic wavefield that spreads through Earth's interior is not a diffuse wavefield, there are other strong reasons for why the thesis about a possible equivalence of the features in global correlograms and the arrivals of body waves in seismic traveltime stacks should be put to a test. To start with, there are many features that show irregular appearances, such as the unusually-high amplitudes of the features that resemble seismic phase ScS ([Boué et al., 2013, 2014](#)). Perhaps more intriguing is that there exist a number of features that appear non-causative (appearing ahead of P waves). Their appearances were puzzling to seismologists and they became known as "spurious" features, a name that has persisted in the literature until recently.

As an initial effort, [Poli et al. \(2017\)](#) presented a plausible explanation for the formation of a couple of correlation features: those that resembled ScS and PKIKPPKIKP phases, which was against the common belief that the body-wave part of the Green's function was reconstructed. Instead, they argued that the features in question were associated with certain high quality factor normal modes. However, this theoretical explanation based on a geometric quantification (a correspondence between each normal mode and a unique family of branching rays) was not applied to other features dominantly observed in the period band of 15–50 s. Further investigation along this line is required to confirm the theory and its actual applications.

Along similar lines, [Pham et al. \(2018\)](#) introduced a convenient explanation for all other features in global correlograms relying on the stationary-phase principle and ray-theory approach. In the following, we review the principle in a slightly different angle from the original paper. A starting point is to recall the stationary-point proof presented in [Wapenaar et al. \(2010\)](#). The stationary point of the correlation traveltime-curve corresponds to the source from which two rays of the same type leave with the same take-off angle (that is, the same horizontal slowness). Fig. A-1 from ([Wapenaar et al., 2010](#)) is slightly modified and presented in [Fig. 3](#) to better fit the content of this section.

The cross-correlation results in the differential traveltime $t_{corr}(x)$ of two contributing phases as a function of a source positioned at position x on the free surface:

$$t_{corr}(x) = t_1(x) - t_2(x), \quad (2)$$

with $t_1(x)$ the traveltime of the ray 1 from the source to the receiver located at point x_1 , and $t_2(x)$ the traveltime of the ray 2 from that source to the receiver located at point x_2 . Note that points x_1 and x_2 are not shown in [Fig. 3A](#) but can be imagined to be placed somewhere on the free surface along the x axis.

To satisfy the stationarity of the cross-correlation traveltime:

$$\frac{\partial t_{corr}(x)}{\partial x} = \frac{\partial t_1(x)}{\partial x} - \frac{\partial t_2(x)}{\partial x} = 0. \quad (3)$$

The relationship between the take-off angle and the horizontal slowness is:

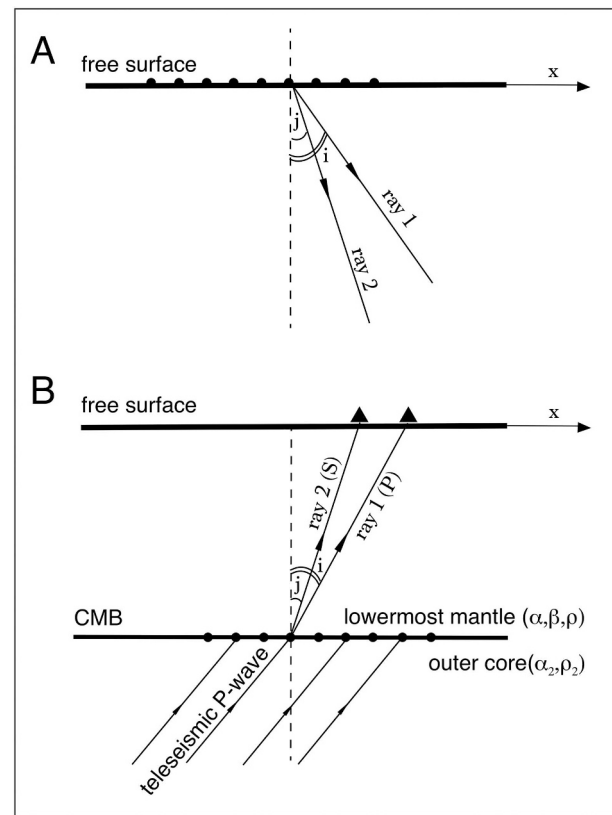


Fig. 3. (A) An illustration of the stationary point principle according to an example given in [Wapenaar et al. \(2010\)](#). A source on the free surface is a stationary point if the two P-wave rays that propagate from the source (dots) have equal take-off angles (leave the source in the same direction). (B) The extension of the stationary principle to the sources at the CMB. Each point at the CMB will act as a stationary point if the two rays, including P- and S-waves, have ratios of take-off angles and the corresponding wave-speed, equal.

$$\frac{\partial t_1(x)}{\partial x} = \frac{\sin i}{\alpha_0}, \quad \frac{\partial t_2(x)}{\partial x} = \frac{\sin j}{\alpha_0} \quad (4)$$

with i the incidence angle of ray 1, j the incidence angle of ray 2 and α_0 the common wave speed of the two rays beneath the surface. Because a similar expression holds for $t_2(x)$, from stationarity, it follows that at the stationary point:

$$i = j, \quad (5)$$

meaning that the rays take-off in the same direction.

[Pham et al. \(2018\)](#) recognized that, within the realm of global interferometry, the core-mantle boundary (CMB) must play a similarly critical role as the free surface of the Earth. The rationale behind that recognition was that the CMB represents a boundary with the most extreme contrasts in elastic properties – in fact, more extreme than the Earth's free surface. It is a thermal boundary that separates two domains: the outer core with vigorous convection, and the slowly-conductive mantle. In addition, the outer and inner cores are exposed to large gravitational and electromagnetic torques due to an asymmetric distribution of the mantle mass and the geomagnetic field. Therefore, it is likely that this boundary can be thought of as a boundary constantly forced by the convective flow from the outer-core side and by seismic waves from large earthquakes, in the same way the free surface is exposed to a constant interaction between the solid Earth and the oceans and atmospheres.

However, our receivers are located 2891 km above the CMB. Given that a thick layer of mantle and crust separates the CMB from the Earth's surface, the seismic wavefield between these two boundaries is exposed to both scattering and intrinsic attenuation due to the Earth's

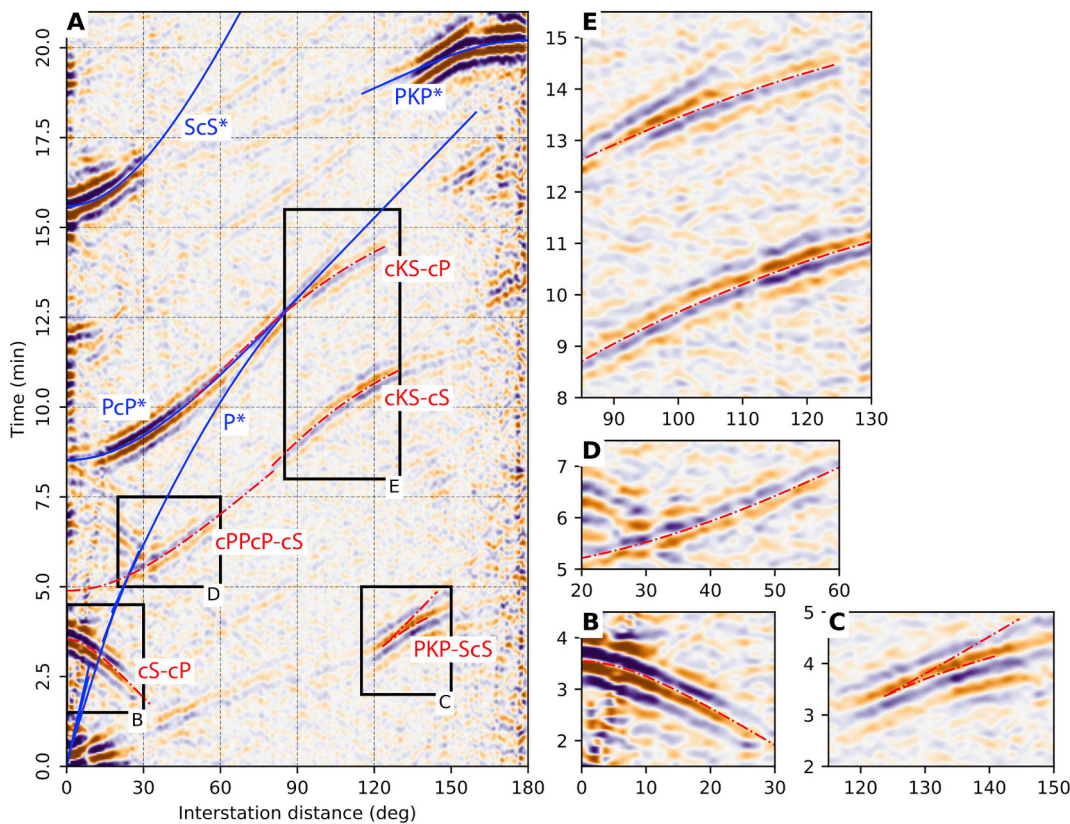


Fig. 4. (A) The first 20 min of the observed cross-correlogram from Fig. 2A showing non-causative and causative (resembling regular phases from the seismic traveltime stacks) features in the Earth's correlation wavefield. The non-causative features are shown in red and the features resembling regular seismic phases are shown in blue. Enlarged sections showing: (B) cS-cP, (C) PKP-ScS, (D) cPPcP-cS, (E) cKS-cP and cKS-cS. Adopted from Phạm et al. (2018). (For interpretation of the references to color in this figure legend, the reader is referred to the web version of this article.)

material properties and it is therefore beyond our capacity to apply the same class of ambient-noise principles and techniques and in the way it is done to image the Earth's subsurface. However, the seismic wavefield after large earthquakes reverberates through the Earth's interior for hours and days despite being attenuated, and there is an omnipresent wave energy arriving at the CMB from both sides. Thus, the CMB can be thought of as a host of infinite number of secondary sources that radiate elastic waves (both P and S types) to the medium on each side of the boundary.

Let us assume an event at teleseismic distances from two receivers on the Earth's surface. Apart from the reflection and refraction, there will be partitioning of energy from P to S waves (Fig. 3B). The horizontal slowness of incoming P waves along the CMB entering the boundary from the core side can be expressed as:

$$\frac{\partial t_p(x)}{\partial x} = r_{CMB} \frac{\sin i}{\alpha}, \quad (6)$$

with r_{CMB} the radius of the CMB, i the incidence angle and α the P-wave velocity above the CMB.

Similarly, the horizontal slowness of S waves converted from P waves along the CMB can be expressed as:

$$\frac{\partial t_s(x)}{\partial x} = r_{CMB} \frac{\sin j}{\beta}, \quad (7)$$

with j the incidence angle of S waves and β the S-wave velocity above the CMB.

Traveltimes $t_{corr}(x)$ of the correlation for a given source position is:

$$t_{corr}(x) = t_s(x) - t_p(x). \quad (8)$$

The condition that the correlation-feature traveltimes is stationary requires:

$$\frac{\partial t_{corr}(x)}{\partial x} = \frac{\partial t_s(x)}{\partial x} - \frac{\partial t_p(x)}{\partial x} = 0. \quad (9)$$

From (6), (7) and (9) it follows that:

$$\frac{\sin i}{\alpha} = \frac{\sin j}{\beta}, \quad (10)$$

which is an equation that is equivalent to Snell's law. This means that the point sources at the CMB exist from which P and S waves are radiated and recorded at the given two receivers on the surface with the same horizontal slowness so that Snell's law is satisfied.

The energy partitioning at the CMB into S waves recorded by one and P waves recorded by the other receiver, results in highly similar waveforms, and the cross-correlation between them produces the non-causal feature cS-cP, whose expression was previously considered a "spurious" signal. The letter 'c' in the newly named feature stands for the CMB, where a subset of common ray propagation-legs eventually splits to S and P waves. Apart from the origin of cS-cP, the study by Phạm et al. (2018) offered an effective conceptual framework for the origin of all prominent non-causal signals including cPPcP-cS, cKS-cS, cKS-cP, and PKP-ScS (Fig. 4). That provided a basis for the explanation of the entire correlogram, including the features that resemble regular phases in the direct seismic wavefield, e.g. P*, PcP*, ScS*, PKP* and others (Fig. 4), which can all be explained based on interferences between body waves of the same slowness. An asterisk is used to distinguish these features from their counterparts in the seismic wavefield; for the naming convention, see Tkalčić and Phạm (2018). To emphasise the difference between the direct seismic wavefield, the term correlation wavefield was coined. Kennett and Phạm, 2018a used the generalised-rays formalism to corroborate the point that all features in the correlation wavefield emerge due to the interaction of arrivals with a

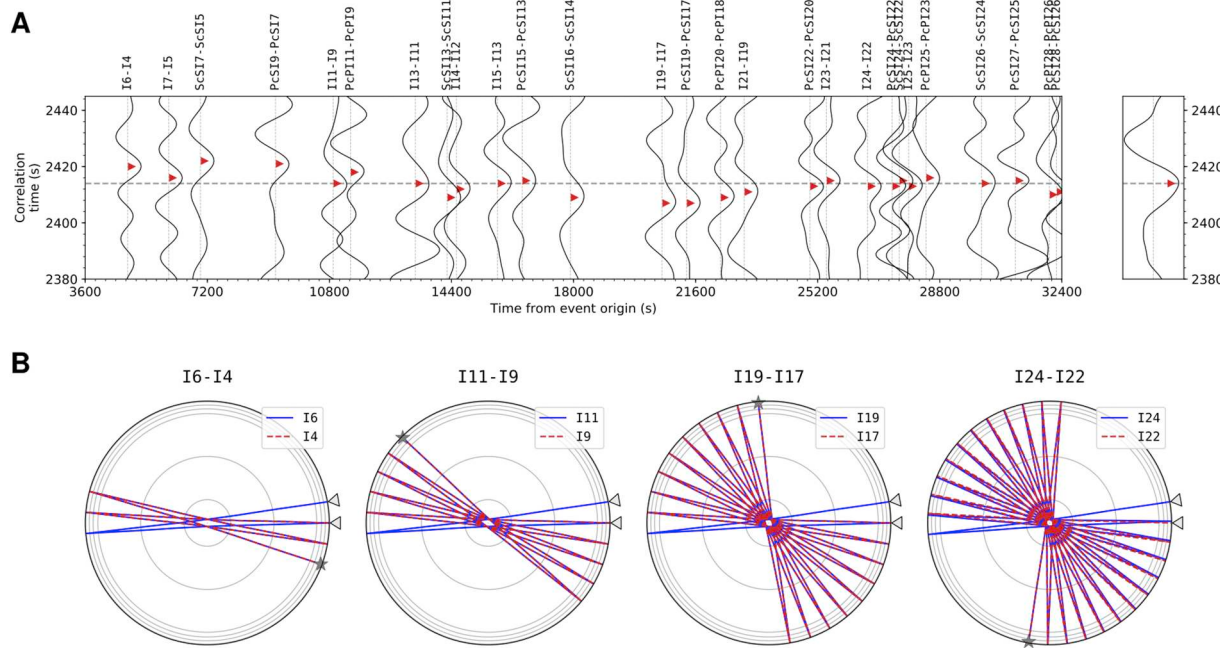


Fig. 5. (A) The formation of the correlation feature $I2^*$. The 1st row demonstrates different body-wave cross-terms as a function of time from event origin. Red arrows show the timing of the negative maxima contributing to the formation of the $I2^*$ cross-correlation peak. The 2nd row shows the ray-paths for the selected constituents of $I2^*$ from the event in the stationary point to the fixed receiver pair: (B) I6-I4, (C) I11-I9, (D) I19-I17 and (E) I24-I22. Adopted from Wang and Tkalcic (2020b). (For interpretation of the references to color in this figure legend, the reader is referred to the web version of this article.)

common horizontal slowness.

Wang and Tkalcic (2020a, 2020b) demonstrated that the main contributions to an individual correlation feature are cross-terms between a few body-wave phases that are mainly reverberations from the Earth's free surface and the CMB. A “dissection” of one such feature, $I2^*$, is shown in Fig. 5. When the cross-correlation functions are shown in a two-dimensional time domain, with horizontal axis showing the time from event origin and vertical axis showing the correlation time (Fig. 5A), it becomes transparent how each of the constituents contribute to their stack, shown in the far right. These constituents are uniquely identified as body-wave pairs of the same (stationarity principle applies) or similar (quasi-stationarity principle applies) slowness, characterized both in terms of their arrival times, energy and coherence, and therefore represent an observational proof of the conjecture presented earlier (Pham et al., 2018). Fig. 5B shows the ray-paths of selected body-wave pairs that contribute to the formation of each constituent to $I2^*$.

The same-slowness condition does not only explain the formation of the correlation features, but it also emphasizes a key difference between the global-scale correlation-wavefield and the cross-correlation of the ambient noise. The former is merely a summation of a finite number of body-wave cross-terms, whereas the latter converges to an inter-receiver medium response, a.k.a. Green's function.

2.4. Observational proof for the formation of global correlation features

Another striking characteristic of global correlograms is that the expression of the correlation features tends to be stronger when the later portions of coda are used (this is illustrated in the Methods section). Highly-prominent features are obtained if the correlogram is formed from the seismograms excised from about 3 h from the event origin time. The effectiveness of the late-coda window has been reported and used in previous studies (Lin and Tsai, 2013; Pham et al., 2018; Poli et al., 2017; Tkalcic and Pham, 2018). Kennett and Pham, 2018b investigated the temporal evolution of the correlation wavefield in different earthquake-coda time segments and offered an explanation that the correlation features are favoured by an increasing number of

contributing body-wave pairs under the same-slowness condition in the late earthquake-coda. Wang and Tkalcic (2020b), however, found that an increasing number of contributing body-wave pairs is not a complete explanation for the growing strength of the correlation features in the late coda.

By decomposing each correlation feature into its constituents, that study presented an observational proof that there are many more significant contributions due to body-wave cross-terms in the late earthquake-coda than in the earlier time windows. Importantly, the cross-terms from the late earthquake-coda exhibit much less time variations than those from early time windows, and hence can constructively interfere in the stacking and correlogram-forming process to form stable and prominent features. For example, Fig. 6A and B demonstrate that the cross-term between I6 and I4 (the constituent I6-I4 of $I2^*$) exhibits time variations up to ~ 60 s due to globally-varied event locations, whereas the cross-term between I22 and I20 (the constituent I22-I20 of $I2^*$) exhibits time variations of ~ 5 s at most. Therefore, if there are no restrictions imposed on the selection of events and receiver pairs, the former distorts the $I2^*$ feature (both in terms of phase and time), whereas the latter constructively contributes to its formation. Fig. 6C illustrates the difference in ray paths of the contributing body waves for a varying source location relative to a given receiver pair. Consequently, adopting the practices from ambient-noise cross-correlation studies to recover the Green's function and utilise the coda-correlation features in a similar way for deep-Earth studies (without event selection) would lead to erroneous interpretations.

Boué et al. (2014) showed that the correlation features that resemble body waves were prone to large time-inaccuracies with respect to the theoretical predictions from spherically-symmetric Earth-models. Wang and Tkalcic (2020a, 2020b) showed that the geometry of the chosen event-locations with respect to the receiver pairs affects the timing of the constituents that form the correlation features. For each contributing constituent, there exists a stationary zone such that the events located in that zone will produce constructively-interfering arrivals (Fig. 6C; left). The events out of the stationary zone (Fig. 6C; middle and right) will distort the travel times of the constituent, thus distorting the shape and prominence of the corresponding correlation

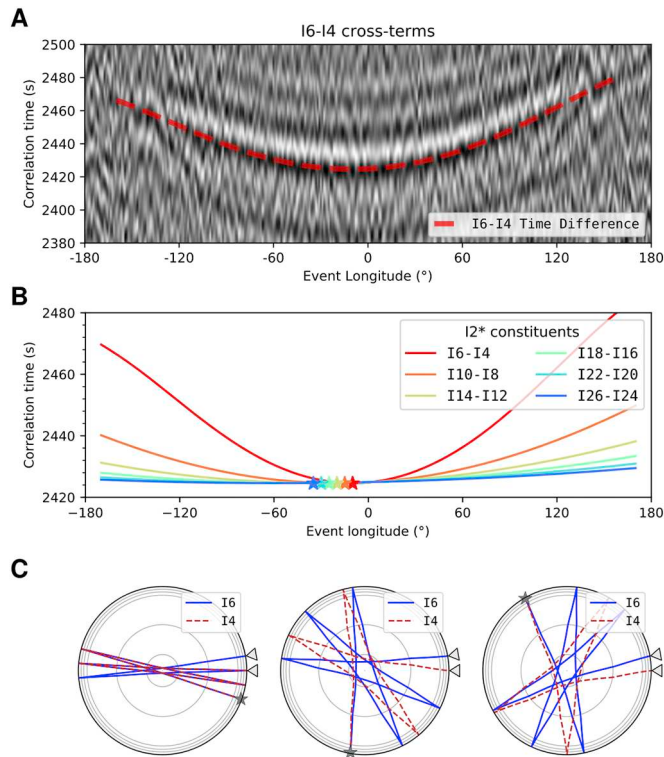


Fig. 6. (A) Arrival time variations for the $I2^*$ constituent I6-I4. (B) Arrival time variations for the selected $I2^*$ constituents due to globally-varied event locations. (C) Left: ray paths for I6 and I4 for the fixed receiver pair and the stationary point event (so that I6 and I4 arrive at the two receivers with the same horizontal slowness). Middle and right: the same as the left column, but the event is located at two randomly-chosen points away from the stationary point. Adopted from Wang and Tkalcic (2020b).

feature. In 3D Earth, there are events outside the great-circle plane shown in Fig. 6, and the seismic wavefield propagation is altered by structural heterogeneity. However, it has been demonstrated via analysing late-coda observations that the events outside the great-circle plane do not contribute significantly to the formation of the correlation features (Wang and Tkalcic, 2020b). Therefore, if restrictions on the selection of events and receiver pairs can be imposed in the data pre-processing stage, the time-inaccuracies with respect to the theoretical predictions based on the ray theory can be significantly suppressed.

3. Data processing methods

3.1. Digital cross-correlation

The central operation in data processing is the cross-correlation function between continuous recordings at two seismic receivers, which is defined as:

$$v[m] = \sum_{\substack{0 \leq i < N \\ 0 \leq m+i < N}} x[i] \cdot y[m+i], \quad (11)$$

where $\{x[i]; i = 0, N-1\}$ and $\{y[i]; i = 0, N-1\}$ are two input waveforms, discrete time series of equal length, N , separated by the time step, m . As we have written in Section 1., the similarity between waveforms is manifested via the cross-correlation functions. This can be used to detect feeble signals in the seismic wavefield that are often overlooked in raw seismograms. In the frequency domain, the cross-correlation function is equivalent to the multiplication of one spectrum and the complex conjugate of the other,

$$\hat{v}[k] = \hat{x}[k] \cdot \hat{y}^*[k] \quad (12)$$

In this equation, $\hat{x}[k]$ and $\hat{y}[k]$ are Fourier transforms of $x[i]$ and $y[i]$ and the superscript * denotes the complex conjugate. Because the Fourier transform can be performed rapidly (Cooley and Tukey, 1965), the cross-correlation function of long seismograms are often computed in the frequency domain.

3.2. Construction of global correlograms

In seismological studies utilising cross-correlation, seismologists benefit from the fact that the number of cross-correlated pairs of seismograms is significantly larger than the number of individual seismograms, and the range of inter-receiver distances is wider than the range of epicentral distance. Forming global correlograms by stacking cross-correlation functions in bins of inter-receiver distance helps greatly in identifying weak correlation features, which otherwise would be difficult to recognise in individual cross-correlation functions.

Bensen et al. (2007) presented a comprehensive overview of the concepts and effects of various processing operators. Despite the fact that the steps were originally designed for extracting surface wave components in ambient-noise studies, they also turned out to be helpful in studying the correlation features in the coda correlograms that resembled body waves, and that were, at least initially, seen as “reconstructed” body waves. In the following, we lay out the data pre-processing and processing procedures utilised to construct global correlograms as presented in Pham et al. (2018). These procedures are designed for studies of multiple correlation features that appear in global correlograms and they include temporal and spectral-normalisation steps before computing the actual cross-correlation function. Readers can find details of similar data processing flows in other studies (e.g., Boué et al., 2014; Lin et al., 2013; Wang et al., 2015).

The data preparation starts with merging segmented waveforms, removing the mean and linear trend. Merged waveforms are then corrected for instrumental response, which can be greatly heterogeneous over networks deployed and operated by various national agencies, to obtain true ground motions, often the velocity component. Then, the waveforms are resampled to a common sampling rate among all stations. In practice, the choice of the sampling rate decides the overall computational time and is empirically set to 10 samples per second.

Fig. 7 summarises the main data processing procedure, which starts with a temporal normalisation operator. This time normalisation mitigates unwanted effects of seismic arrivals of possible early aftershocks or instrumental glitches. For this purpose, we use the running-absolute mean normalisation as it effectively suppresses the anomalous waveform amplitudes while retaining the shape of the waveform. In this operation, an adaptive normalisation weight, $d[n]$, is calculated as the running-average mean of the pre-filtered waveform,

$$d[n] = \frac{1}{2N+1} \sum_{j=n-N}^{n+N} |\bar{x}[j]|, \quad (13)$$

where $\bar{x}[n]$ is the zero-phase bandpass-filtered waveform of the original waveform $x[n]$ and $|\cdot|$ is the absolute value operator. There are two parameters to empirically tune in the previously-described steps including the filtering frequency-band of the weight, and temporal normalisation width, $\Delta W = 2N\Delta t$, where Δt is the time step of the input waveforms. Empirically, the pre-filtering band to compute the weighting factor is set to 15–50 s, and the temporal normalisation width is set to 128 s (e.g., see F.-C. Lin et al., 2007; Pham et al., 2018). The weight computed from the pre-filtered waveform as in Eq. (13) is more effective than the weight factor from the unfiltered waveform in suppressing unwanted aftershock signals in their dominant-frequency band. A deeper discussion on advantages of this operator can be found in Bensen et al. (2007). In Fig. 7A, the adaptive weights of the two input waveforms are shown as gray waveforms, while the original unfiltered waveforms are in black. The temporally-normalised traces are obtained by dividing the original waveforms by the normalisation weights:

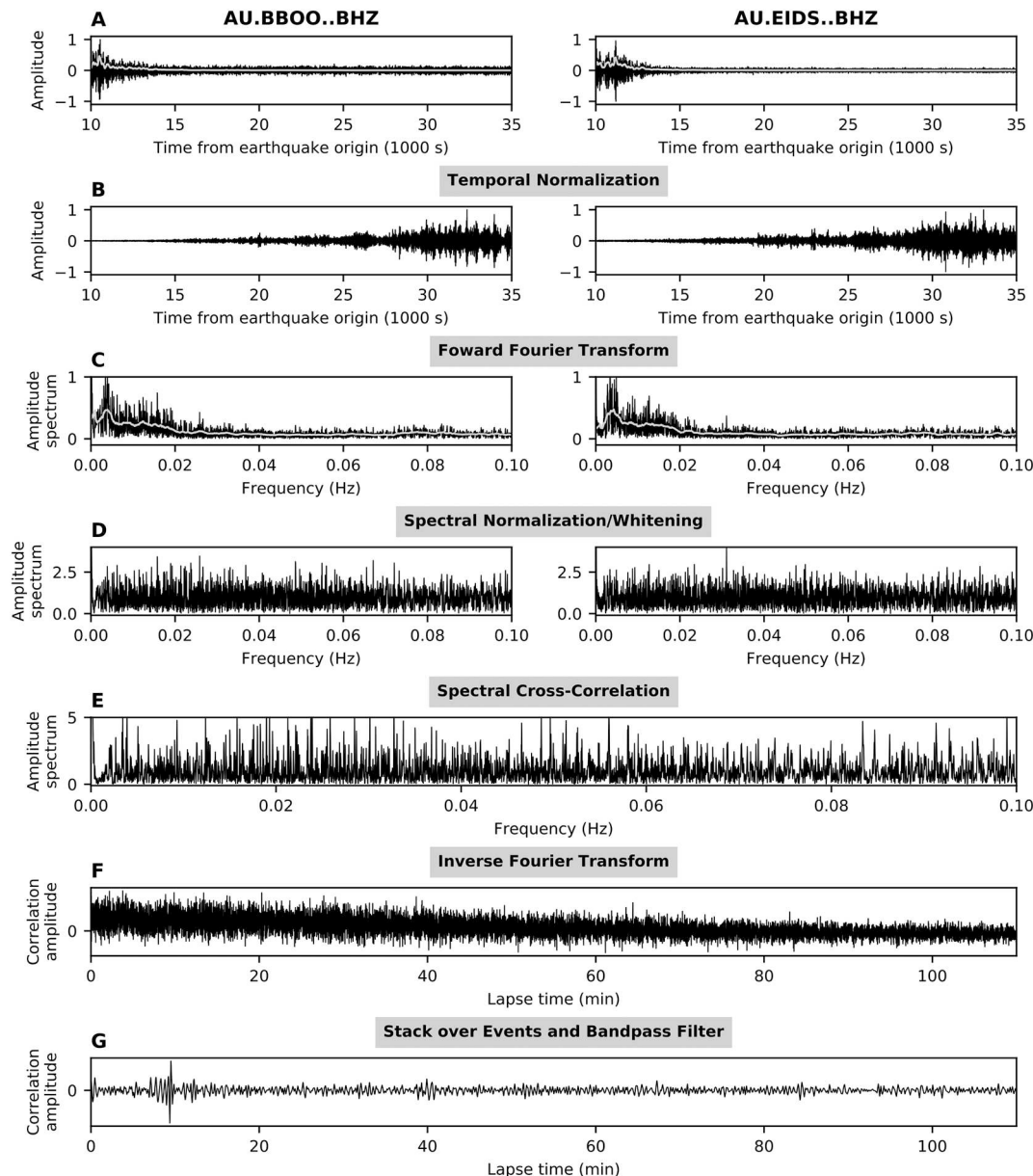


Fig. 7. Coda correlation data processing flow. (A) Black traces are original velocity seismograms of the Mw 7.1, Oct 212,011, earthquake in Kermadec Islands registered by two stations in Australia. Gray traces are the running average computed adaptively as the weight factor for the temporal normalisation performed in the next step. (B) Temporally-normalised seismograms derived by dividing the original seismograms with the running average weight. (C) Black traces are the spectra of the normalised seismograms. Gray traces are the running average of the original spectra as the weight for the spectral normalisation/whitening performed in the next step. (D) Whitened spectra derived by dividing the original spectral by the running average weight traces. (E) Spectral cross-correlation as multiplication of whitened spectra. (F) Temporal cross-correlation computed by inverse Fourier Transform the spectral cross-correlation. The cross-correlation is folded at time 0 s to yield the symmetric correlation. (G) Correlation stack over earthquakes for the pair of station. The correlation stack is filtered in 15–50 s period band (zero phase).

$$\hat{x}[n] = \frac{x[n]}{d[n]}, \quad (14)$$

and they are shown in Fig. 7B.

The temporal normalisation is followed by a spectral normalisation. Temporally-normalised waveforms in the previous step are first Fourier-transformed to the frequency domain (Fig. 7C). The normalisation in frequency domain balances the contribution of the individual frequencies in the cross-correlation. The form of the spectral normalisation is similar to the running-absolute normalisation in the time domain (Bensen et al., 2007; F.-C. Lin et al., 2007),

$$\hat{s}[m] = \frac{s[m]}{\frac{1}{2N+1} \sum_{j=m-N}^{m+N} |s[j]|}, \quad (15)$$

where $s[m]$ is the complex spectra of the input signals. When $N = 0$, the resulting spectra are completely white, or the amplitude spectrum is homogeneously flattened to 1. Fig. 7D shows the whitened spectra of input waveforms. Pham et al. (2018) empirically used the spectral whitening width of 2 mHz.

In the following stage of the data processing, single-receiver processed waveforms are cross-correlated and stacked in inter-receiver distance-bins to construct a two-dimensional correlogram. As mentioned before, the cross-correlation in the time domain is equivalent to the multiplication of one spectrum and the complex-conjugate of the other. Spectral correlation can be readily computed from the pre-computed whitened spectra from the previous step. An example of the cross-correlation function in the frequency domain is shown in Fig. 7E. After an inverse Fourier transform is applied (Fig. 7F), we obtain the

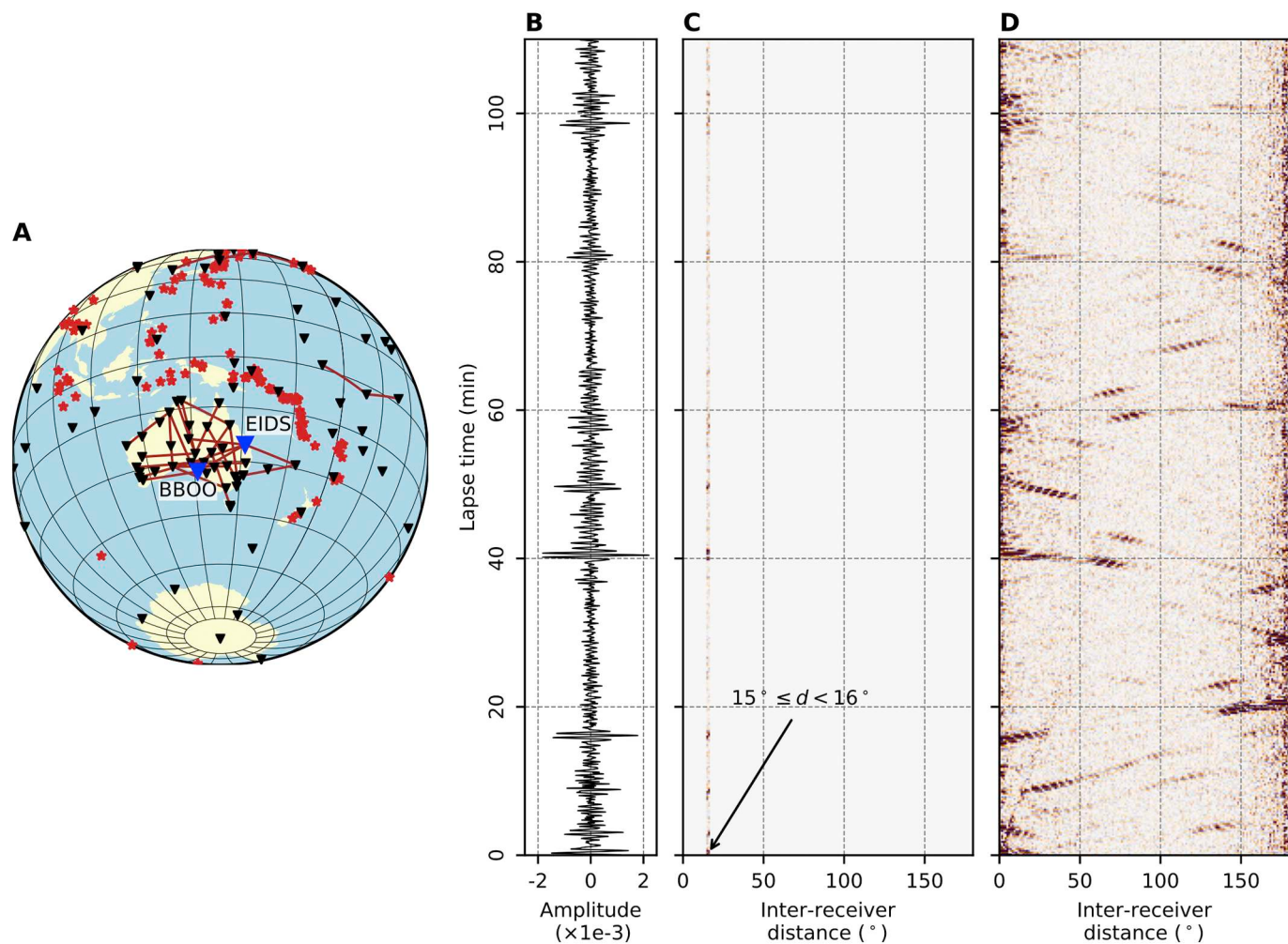


Fig. 8. Construction of a global correlogram through stacking correlation in inter-receiver angular-distance bins. (A) Map of earthquakes and stations in the Australasian region used to illustrate the construction of a global correlogram. Brow lines connect receiver pairs with inter-received distances falling in the bin between 15 and 16°. Inverted black triangles show stations in the Global Seismograph Network (network codes: II/IU) and the Australian Seismograph Network (network code: AU). Blue triangles marks the two stations that have data shown in 8G. (B) Correlation waveform stack over all earthquakes and all station pairs in the bin 15°–16°. (C) Interim correlogram with the correlation waveform stack shown as a color-coded strip in the two-dimensional image. (D) Final global correlogram over the full range of inter-receiver distances (0–180°). (For interpretation of the references to color in this figure legend, the reader is referred to the web version of this article.)

cross-correlation function in the time domain. The correlation function in time is then folded at the time zero to yield a symmetric correlation function. Finally, for the same receiver pair, multiple cross-correlations corresponding to the coda of large earthquakes can be stacked and band-pass filtered (Fig. 7G) in the period range 15–50 s, and this represents an input into the next stage of data processing.

In global studies, there are often two stacking steps to enhance the signal-to-noise of final correlation products. EIDS and BBOO station locations in Australia distanced from each other by 15.5° were chosen here as an example for the receiver pair falling in the epicentral-distance bin $15^\circ \leq d \leq 16^\circ$ (Fig. 8A). Apart from stacking cross-correlations calculated from multiple earthquakes (red stars in the same figure), we further stack all receiver pairs whose angular distance falls into the inter-receiver distance bin $15^\circ \leq d \leq 16^\circ$ (Fig. 8B). The binned cross-correlation stack is then color-coded (purple for negative and orange for positive amplitudes) as a strip in the lapse-time – inter-receiver-distance domain (Fig. 8C). The global correlogram is completed when all inter-receiver bins are considered, cross-correlations calculated, and the corresponding strips assembled (Fig. 8D).

3.3. Input-data selection: late coda of large earthquakes

The data-processing presented in the previous section can be applied to any simultaneously-recorded seismic records by regional or global seismic networks. In this section, we review the relative importance of assembling a large volume of earthquake data as an input for extracting global correlation features.

Early attempts to construct global correlograms (Boué et al., 2013; Nishida, 2013) made use of continuous ambient-noise records. However, due to the large volume of seismic data determined by the length of the records and the number of recordings, there has been a high demand of computational resources to perform the task. Several groups (Fichtner et al., 2017; Ventosa et al., 2019) have recently designed advanced computational scheme deployed on HPC cluster for the ambient noise processing. The advanced computational resources might not be available for all researchers, so there is a need to refine the dataset.

Along the lines of reducing long time-series, it was found that the correlation features can be efficiently extracted from the late coda of

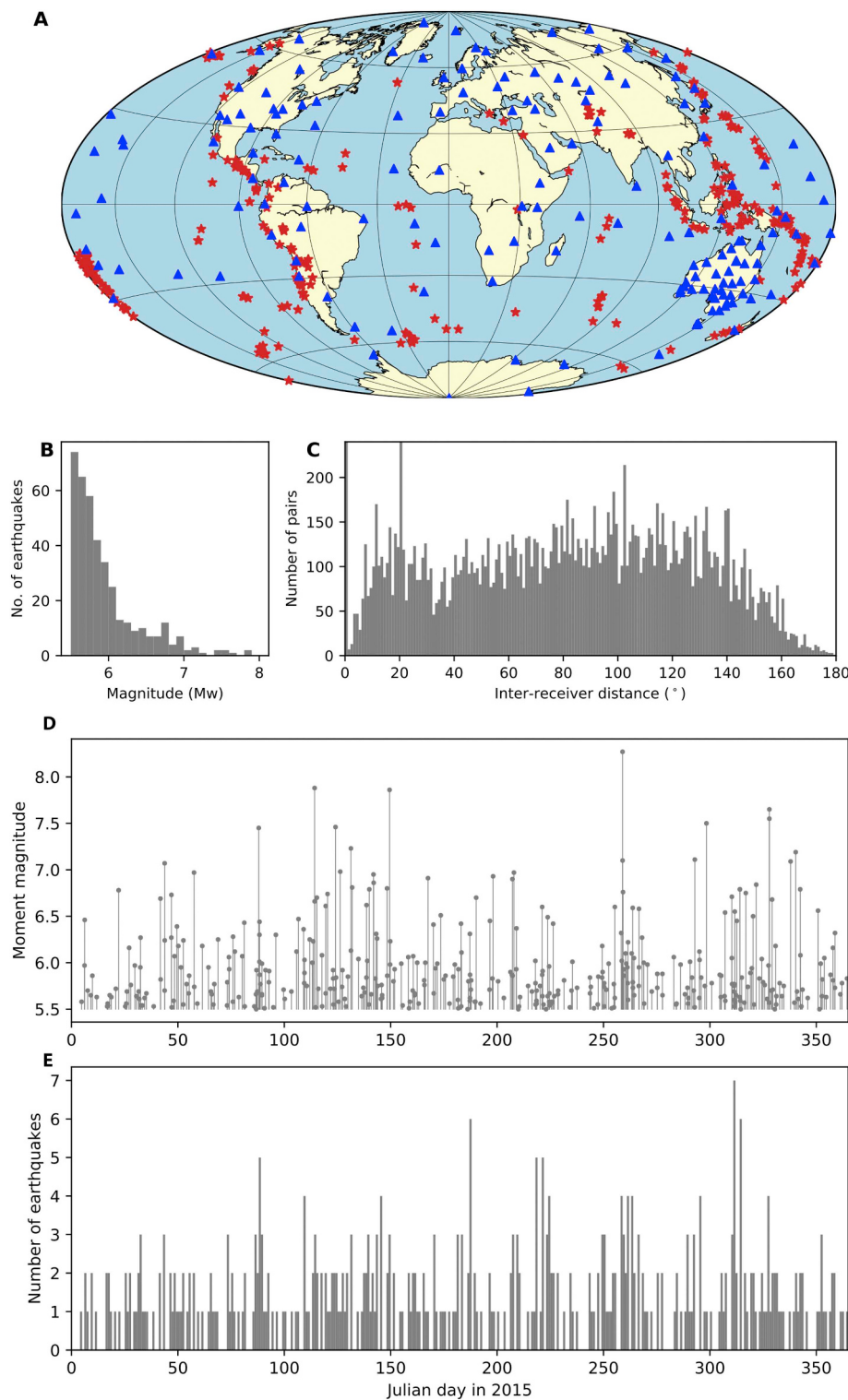


Fig. 9. Global map of earthquakes and stations. (A) Blue triangles mark seismic stations from Global Seismograph Network (network codes: II, IU) and Australian Seismograph Network (network code: AU) are marked by blue triangles. Red stars denote 2015 earthquakes of $M_w \geq 5.5$ from above in the Global CMT catalogue. (B) Number of earthquakes ($M_w \geq 5.5$) in year 2015 plotted as function of moment magnitudes. (C) Number of stations pairs combined over two networks as a function of inter-receiver distances with the bin size of 1° . (D) Earthquake magnitudes in 2015 as function of origin time. (E) Number of earthquakes $M_w \geq 5.5$ in each Julian day in 2015. (For interpretation of the references to color in this figure legend, the reader is referred to the web version of this article.)

large earthquakes. Lin and Tsai (2013) showed that several seismic core-phases emerged in the cross-correlation of late records of a large earthquake registered by a pair of nearly-antipodal receivers. Lin et al. (2013) further demonstrated that several deep-Earth phases, including those that are rarely observed in a direct seismic-wavefield, “emerge” in the stack of correlation functions made from a regional seismic-array. By dividing the continuous dataset at a global network by the level of seismicity, Boué et al. (2014) showed the causative relationship between the emergence of long-period correlation features and the level of global seismicity.

In this section, we revisit the previous results by performing a set of experiments in order to characterise major contributions to the formation of global correlation-features. A complete understanding of the factors that determine the clarity of the correlograms would help to greatly reduce the volume of dataset and computational resources involved in future cross-correlation analyses. In order to do so, we work with the seismic data collected in year 2015 from 165 stations of the Global Seismograph Network (network code II, IU) and Australian National Seismograph Network (network code AU). Fig. 9A shows these networks and earthquakes of $M_w \geq 5.5$ recorded in 2015 from the

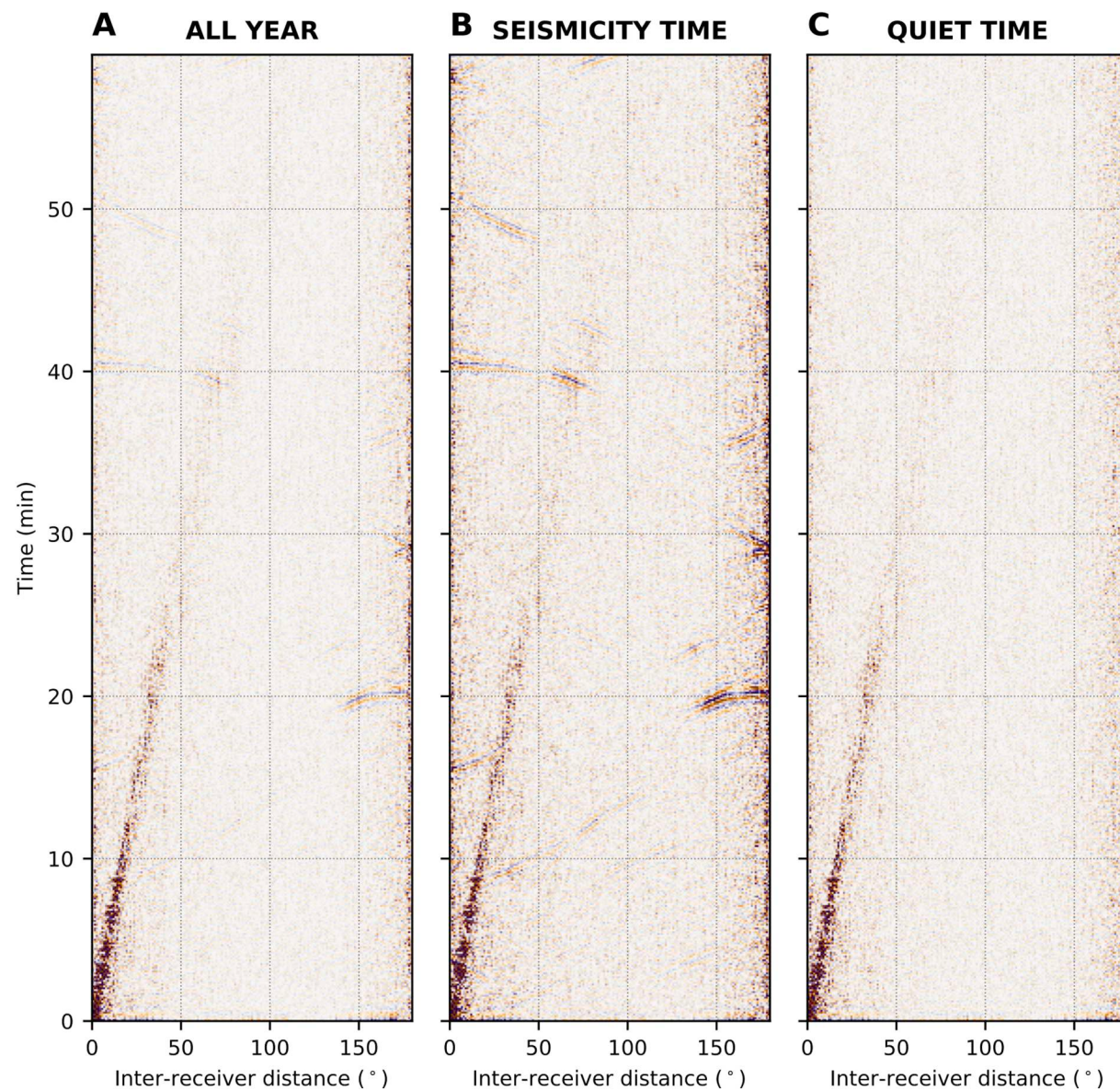


Fig. 10. Illustration of the role seismicity plays in the formation of the correlation features. Data used in the construction of these correlograms are $Mw \geq 5.5$ earthquakes from 2015 recorded by 165 receivers of Global Seismograph Network and Australian National Seismograph Network (see Fig. 10). Continuous data are divided into $365 \times 6 = 2190$ disjoint 4-h windows. (A) Correlogram stacked over all time windows in 2015. (B) Correlogram constructed from the windows associated with seismicity (for the definition of seismicity, see the main text). (C) Correlogram constructed from the windows without significant seismicity.

Global CMT catalogue (Ekström et al., 2012). Frequency histograms in Fig. 9B and C further demonstrate the distributions of large earthquakes in magnitude bins and the number of receiver pairs in each inter-receiver distance bin. Note that the bimodal distribution in Fig. 9C stems from the inclusion of the AU regional network, hence more receiver pairs are available in short inter-receiver distances.

In the following sections, we investigate the contribution of “seismicity” versus “pure ambient noise” to the global correlogram. Subsequently, we consider the magnitude threshold, source mechanisms and optimal time-window used in correlation analysis.

3.3.1. Contribution of seismicity

We divide the continuous dataset from 2015 into $365 \times 6 = 2190$ disjoint windows, and construct a correlogram for each 4-h long window. Individual correlograms are then stacked into two complementary groups: the first group is related to earthquake events, and we refer to it as “seismicity-time stack”, and the other is not related to any significant seismic activity and we refer to it as “quiet-time stack”.

More specifically, a time window is classified as the seismically-active time and placed in the seismicity-time stack if there is an occurrence of an $Mw \geq 5.5$ earthquake either during this window or in two preceding windows. The assumption we make is that if there are no earthquakes that fit our seismicity criteria, the corresponding time windows are grouped in the “quiet stack” and they presumably represent only non-transient background noise. Fig. 9D and E help appreciate the distribution and frequency of significant earthquakes ($Mw \geq 5.5$) as a function of Julian day in 2015.

The dominant contribution of seismicity to the formation of the correlogram features is clearly demonstrated in Fig. 10. Correlation features can be seen in the “all-year” stack (Fig. 10A), but they appear with a significantly higher visibility in the “seismicity-time” stack (Fig. 10B). There are no visible correlation features in the “quiet-time” stack apart from surface wave trains near the lower left of the correlograms (Fig. 10C). Our results corroborate some of the findings of Boué et al. (2014). In their experiment, the category of high-coherence days (HCD) is related to major seismic activities. However, they based their

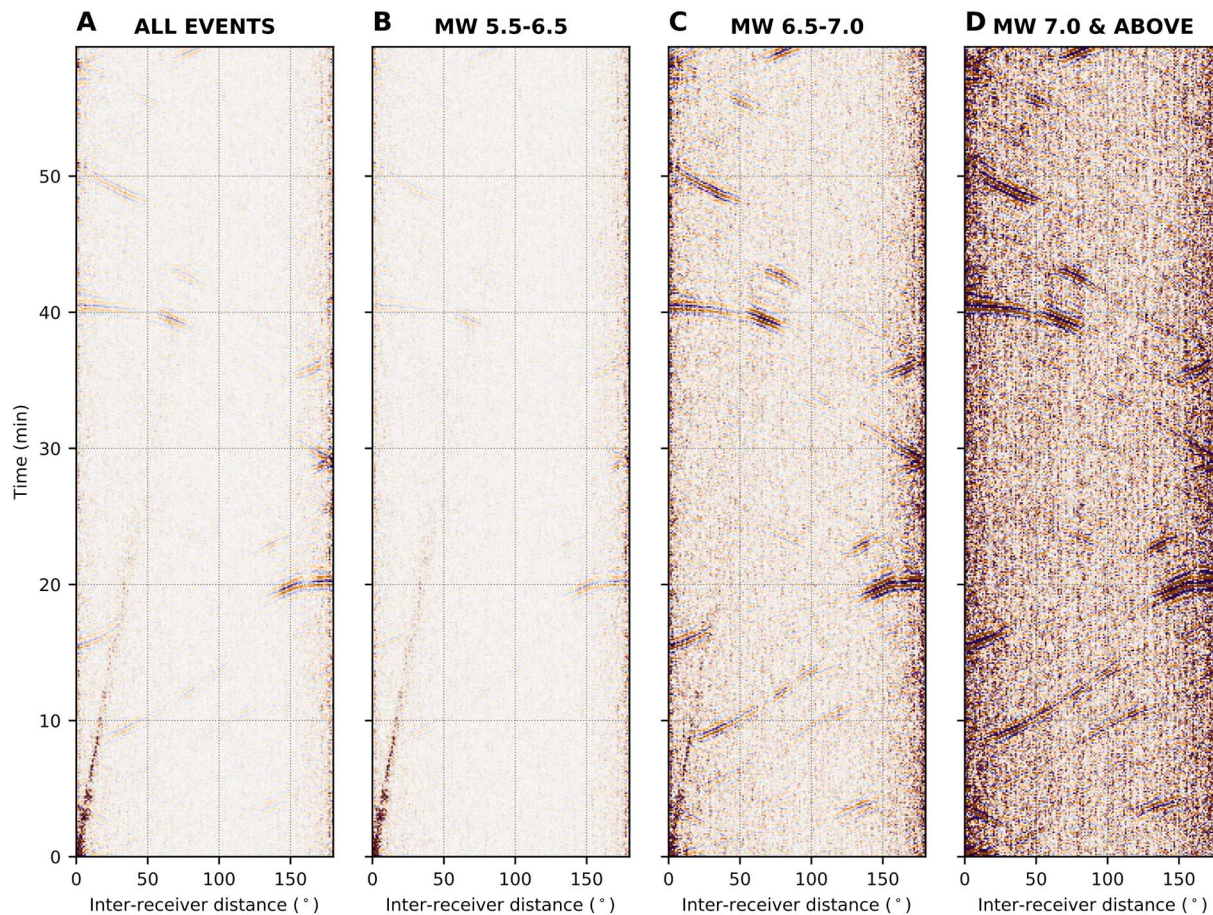


Fig. 11. Correlograms constructed from the events of different magnitudes. 3–10-h time-windows after the origin time are used in the construction. The following magnitude ranges are used: (A) All events with $Mw \geq 5.5$. (B) $5.5 \leq Mw \leq 6.5$. (C) $6.5 \leq Mw \leq 7.0$. (D) $Mw > 7.0$.

selection on the coherency of several correlation features with a “master” correlogram, therefore there are days with high level of seismicity that fall into low-coherence day (LCD) category. This is the most likely explanation for the weak appearance of the correlation features in their LCD stack, while they are absent in our “quite-time” correlogram sorted by catalogued events.

The absence of the correlogram features in Fig. 10C is in agreement with the conceptual framework around the formation of the correlation features presented in Section 2. It demonstrates that the body waves do not “emerge” by a virtue of Green’s function reconstruction in the same way surface waves emerge in the presence of diffuse, ambient-noise wavefield.

3.3.2. Earthquake magnitude

In our next experiment, we further investigate the level of contribution of seismicity by considering different magnitude brackets. Individual correlograms for each $Mw \geq 5.5$ event in 2015 is constructed using the time window from 3 to 10 h after the origin time. The choice of this window will be clarified in Section 3.3.4. Fig. 11 shows correlograms for all earthquakes and for three specific subsets or earthquake-magnitude brackets, $Mw < 6.5$, $6.5 \leq Mw < 7.0$ and $Mw \geq 7.0$. Many first-order correlation features can be seen in all correlograms with different levels of visibility. Note that the larger background noise in the case of $Mw \geq 7.0$ earthquakes is due to the fact that there are only few events in this bin (see magnitude histogram in Fig. 9B). The correlogram stacks for groups of $6.5 \leq Mw < 7$ and $Mw \geq 7.0$ express

higher-quality correlation-features even though there are much less events in these stacks than in the correlogram made of smaller-magnitude events (see the histogram of earthquake magnitude in Fig. 9B). This reconfirms the contribution of seismicity to the formation of global correlation-features.

3.3.3. Earthquake mechanism

In this experiment, we consider the contribution of different source mechanisms on the formation of features in global correlograms constructed from 3 to 10 h after origin times. From the focal mechanism solutions obtained from the GCMT catalogue (Ekström et al., 2012), we place all earthquakes satisfying the magnitude condition $Mw \geq 6.5$ in 2015 into three groups: thrust-faulting events, strike-slip events and normal faulting events. The classification is based on the plunge angles of tension and the null axes computed from the published solutions. Out of 55 events satisfying the magnitude threshold, there are 21 strike-slip events that have large plunge of the null axis ($> 45^\circ$), 24 thrust-faulting events that have large plunge of the tension axis ($> 45^\circ$), and 10 normal-faulting events that have small plunges for both null and tension axes.

We plotted a summary comparison of the correlogram made up of all 55 events (Fig. 12A), and the correlograms made from the events classified in sub-groups according to the description above (Figs. 12B–D). Despite the fact that there are comparable numbers of earthquakes in each sub-group, the first-order features, such as I1*, I2*, cKc*, are just weakly expressed in the strike-slip correlograms

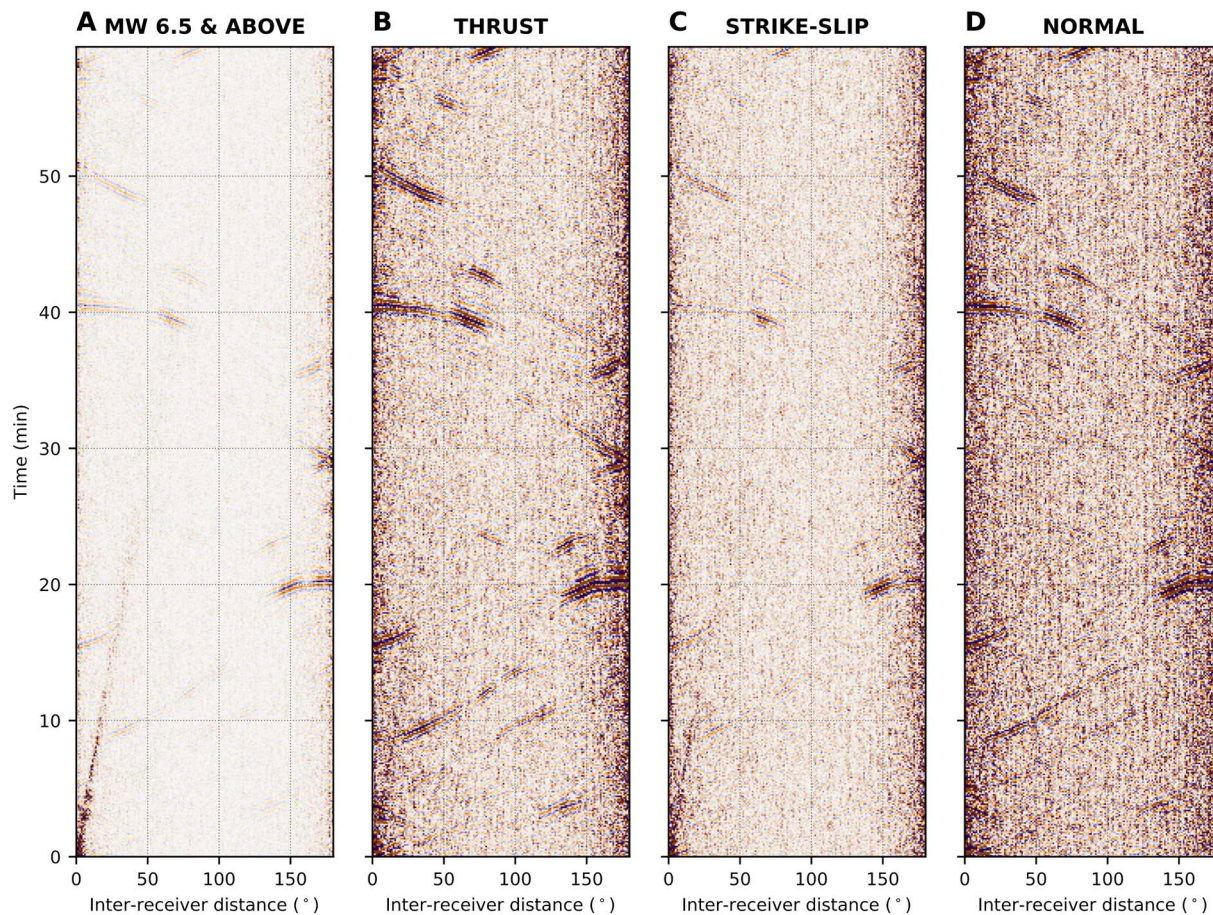


Fig. 12. Correlograms constructed from the events of different focal mechanisms. 3–10-h time-windows after the origin time are used in the construction. (A) All events with $M_w \geq 6.5$. (B) Thrust faulting earthquakes, which have large plunge of the tension axis ($> 45^\circ$). (C) Strike-slip earthquakes, which have large plunge of the null axis ($> 45^\circ$). (D) Normal faulting earthquakes, which have small plunges for both null and tension axes.

(Fig. 12C), while many more correlation features are prominent in thrust and normal faulting groups (Figs. 12B and D). The thrusting and normal mechanisms release a significant portion of seismic energy steeply to the Earth's centre, which helps illuminating the Earth's deep interior. These results are in alignment with previous findings by Xia et al. (2016) who analysed the contribution of source mechanism to the emergence of features similar to PKP triplications in the correlation wavefield.

It can be concluded from these experiments that the correlation features present in global correlograms must be associated with seismic events that release a significant amount of energy to the Earth's deep interior. The suitable candidates are large dip-slip earthquakes, but there are also effects of the complexity of the source-time functions that should be taken into account (Tkalcic and Pham, 2020). Solely ambient noise dominated by near-surface-travelling energy is unlikely to excite the correlation features related to the deep Earth in this frequency range (15–50 s) for the realistic noise conditions of the Earth. However, there have been recent observations of oceanic-microseism noise-sources at higher frequencies (~6 s) that can produce P-type body waves (Li et al., 2020).

3.3.4. Selection of coda window

To test the evolution of the correlation features in time, we use the same set of 55 earthquakes satisfying the magnitude condition $M_w \geq 6.5$ that occurred during 2015. 12-h-long seismograms are cut

into four windows, each 3 h long, starting from the origin time. Stacked correlograms over the events are then constructed from each time window and plotted in Fig. 13. The correlation features are not visible in the correlogram constructed from the first 3 h of seismograms after the origin time (Fig. 13A), but they become prominent in the following correlograms made up from 3 to 6 (Fig. 13B) and 6–9 h windows (Fig. 13C). Finally, the correlation features fade away in the correlogram constructed from seismograms in the late, 9–12-h window (Fig. 13D). This result agrees well with previous studies (Lin et al., 2013; Wang et al., 2015), in which they searched for optimal coda windows based on the expression of several individual correlation-features. A similar conclusion was reached by Kennett and Pham, 2018b when analysing the evolution of correlation features by utilising synthetic seismograms, but the correlation features emerged earlier – after about 2 h.

3.3.5. Properties of late earthquake-coda

As the above analysis suggests, the optimal dataset for global correlation studies that involve deep Earth structure is the late coda of large earthquakes. Sens-Schönfelder et al. (2015) presented an important survey of properties of the late earthquake-coda that shed light on common characteristics of features in the correlation wavefield. According to their study, the late coda consists mostly of intermediate-period reverberations from the Earth's core and long-period free-oscillations of the Earth. The intermediate-period energy keeps propagating

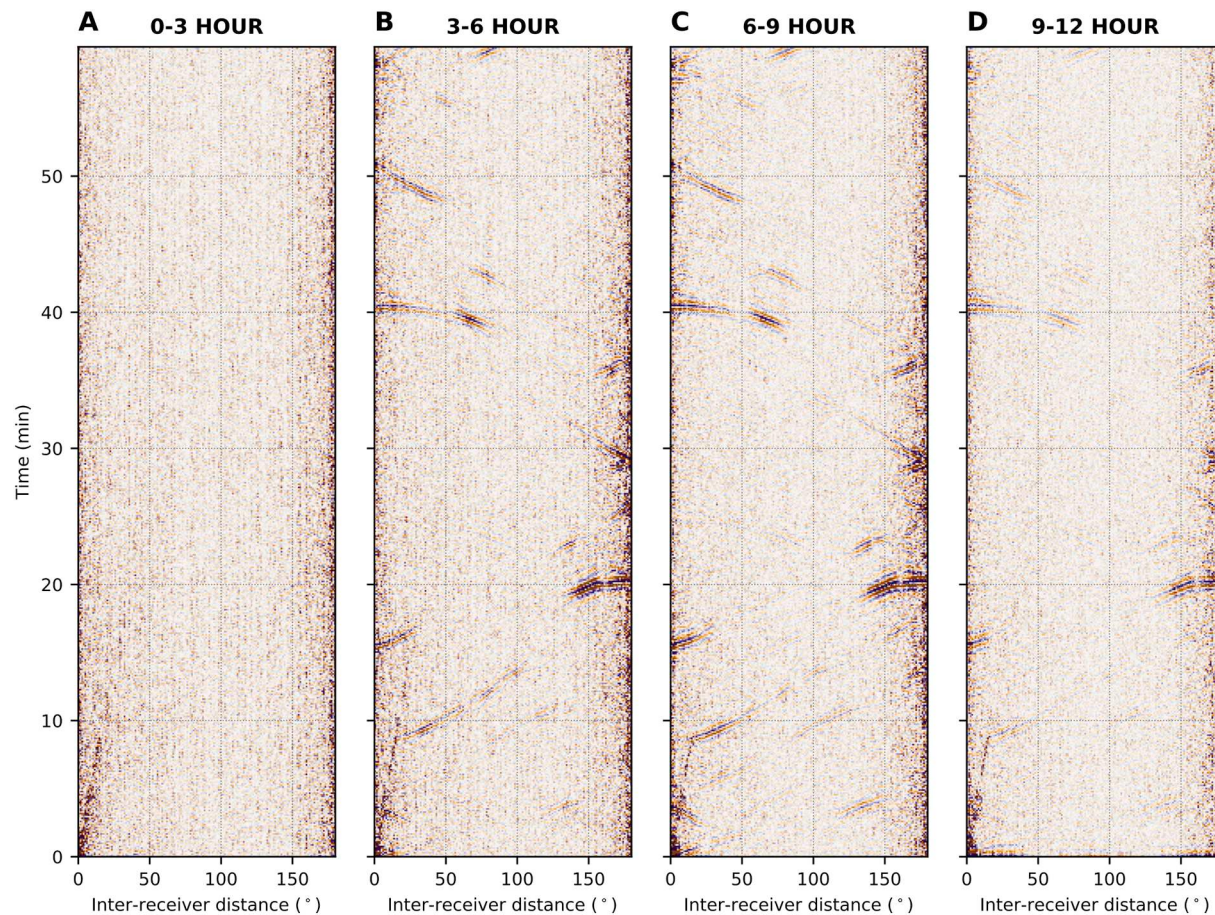


Fig. 13. Correlograms constructed from $55 \text{ Mw} \geq 6.5$ events in 2015 for four subsequent coda-windows, each 3 h long, starting at the event origin time. a) 0–3 h from origin time. b) 3–6 h from origin time. c) 6–9 h from origin time. d) 9–12 h from origin time.

in the initial direction and does not evolve to the randomly-scattered regime. Consequently, the energy is concentrated along the great-circle path from the origin to the observing seismic network. Fig. 14 reproduces the experiment from Sens-Schönfelder et al. (2015), showing the concentration of energy up to 10 h along the great-circle path from a large earthquake in the Sea of Okhotsk (24-May-2013; the red star in the inset of Fig. 14A) recorded by a dense portion of the Transportable Array in Eastern US (yellow triangles). Fig. 14B shows slowness maps measured by the f-k method in different time windows since the event origin time. It is evident that, as time progresses, the steeper seismic-energy reverberations characterized by near-zero slowness get more dominant. This is due to the fact that the CMB and the Earth's free-surface are two efficient reflectors which act as a wave guide for steep-energy reverberation. The energy is more concentrated but also more circular, meaning there is more energy arriving from off the great circle path. Additionally, near-vertical reverberation is less dissipated in time than near-horizontally travelling energy characterized by relatively large slowness due to weaker attenuation at depth.

The properties mentioned above shed light on several common characteristics of correlation features observed to date. Event-coda correlation features are often observed at mid-range period of 15–50 s. There are a few reports of short-period features (Boué et al., 2014; Xia et al., 2016), but they are not regarded as related to the late earthquake-coda. Most significant correlation features have small ray-parameters. The prominent features at antipodal and zero inter-receiver distances (from autocorrelation) can easily be formed due to the fact that the

receiver pairs are by definition on a great-circle path from any of the earthquakes (Sens-Schönfelder et al., 2015).

3.4. Observed and theoretical travel-time curves of correlation features

Many correlogram features have timing properties similar to regular seismic-phases originated from a surface focus. Prominent examples include ScS* in the near-zero inter-received distance range and I2* in the antipodal inter-receiver range. Their theoretical traveltimes can be routinely generated by existing tools such as the Taup Toolkit (Crotwell et al., 1999) or its Python version implemented in Obspy package (Krischer et al., 2015). However, to predict the arrival times of the correlogram features whose timing properties are fundamentally different from regular seismic-phases requires a new scheme. Pham et al. (2018) devised a technique to generate the prediction curves based on the conceptual framework that the correlation features result from the waveform similarity between regular phases that have a common horizontal slowness (ray parameter). Here, for the purposes of this review, we revisit the proposed technique and present a demonstration for calculating the theoretical-prediction curve for the correlation feature PKP-ScS, which is a prominent feature in the lower right of the global correlogram (Fig. 4).

According to the ray theory, travel time and angular (epicentral) distance of a ray-path can be expressed as functions of the ray parameter — p , or equivalently, its take-off angle (e.g., Stein and Wysession, 2003). A travel time curve of a phase X in the time-angular distance

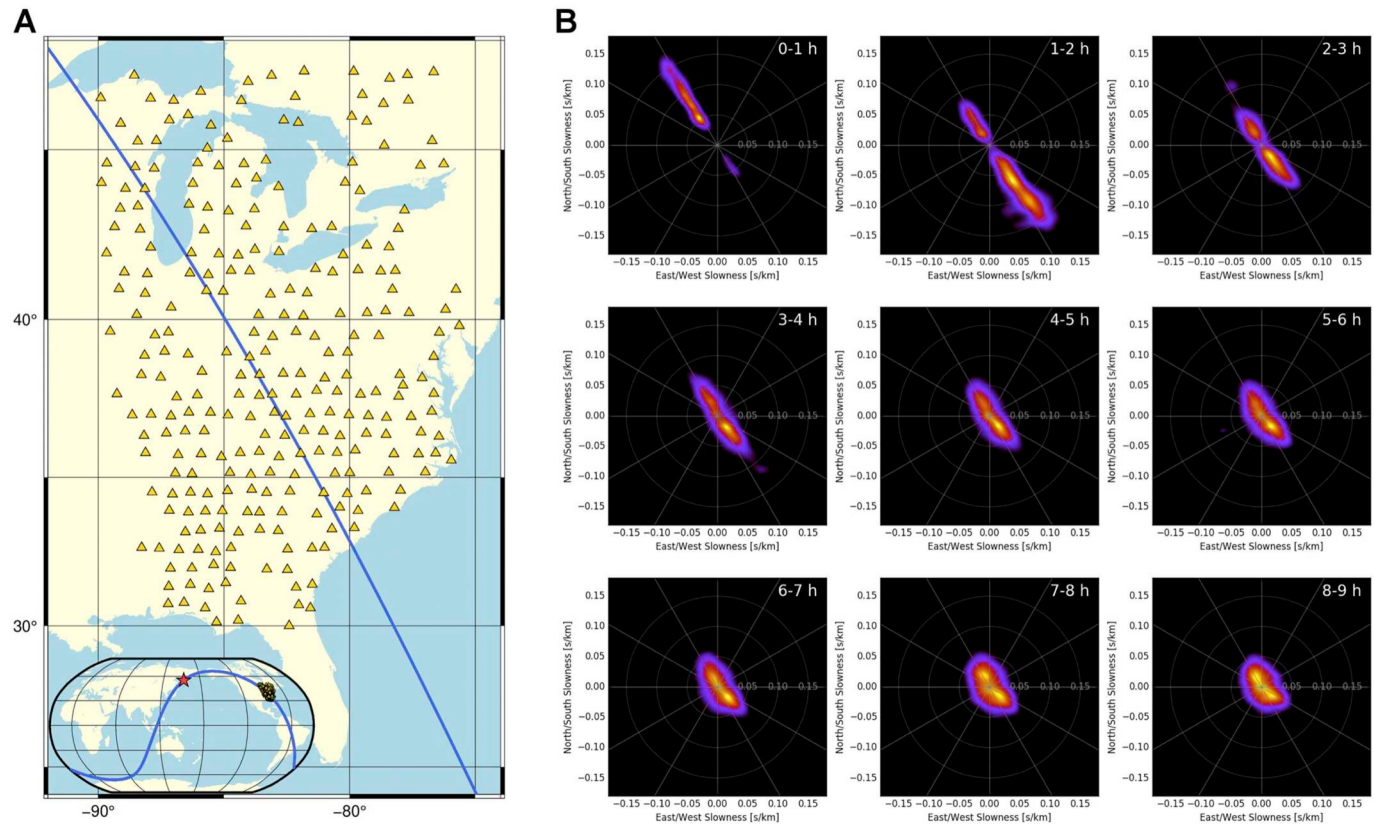


Fig. 14. Slowness maps measured by f-k method at USAarray for Okhotsk earthquake (24-May-2013). (A) Distributions of USAarray stations (yellow triangles) and the great circle path (blue line) from the event (red star) to the network. (B) Slowness maps in different time windows. Different time windows are 0–1, 1–2, 2–3, ..., 8–9 h since the event origin time. (For interpretation of the references to color in this figure legend, the reader is referred to the web version of this article.)

space can be described as a parametric curve of the ray parameter, $t_X(p)$ versus $\Delta_X(p)$. The ray parameter at a given angular distance is the slope of the travel time curve $p = \delta t/\delta\Delta$. The travel time and angular distance of the correlation feature PKP-ScS can then be obtained by subtracting the terms from the contributing pair of seismic phases with respect to the ray parameter (see Fig. 15),

$$\begin{aligned} t_{PKP-ScS}(p) &= t_{PKP}(p) - t_{ScS}(p) \\ \Delta_{PKP-ScS}(p) &= \Delta_{PKP}(p) - \Delta_{ScS}(p). \end{aligned} \quad (16)$$

In practice, Pham et al. (2018) used the SeismicPhase module in the Taup Toolkit (Crotwell et al., 1999), which implements the algorithm of Buland & Chapman (1983), to obtain the travel times, epicentral distances and ray parameters of regular seismic phases. They are stored as three arrays of discrete values. Fig. 15 illustrates the steps in the calculation in the clockwise direction: from the time-distance domain, it is possible to transit to the distance- and time-ray-parameter domains for each branch, and then through the subtractions in Eq. (16), for the same set of ray parameters, a transfer is made back to the time-distance domain.

A similar differential calculation is applied to compute the travel time curves for other differential correlation phases including cS-cP (by means of, e.g., PcS-PcP), cPPcP-cS (by means of, e.g., PcPPcP-PcS), cKS-cS (by means of, e.g., PKS-PcS), cKS-cP (by means of, e.g., PKS-PcP) in Fig. 4. The derived traveltimes provide excellent fits to the observed correlation features. This technique has been an important tool to explore weakly expressed features in the correlation wavefield. For example, Tkalcic and Pham (2018) used it to search for the presence of

the inner-core shear-waves, PKJKP, in the global correlation wavefield. Using the existing spherically-symmetric models of the Earth, i.e. ak135 (Kennett et al., 1995) or PREM (Dziewoński and Anderson, 1981) is appropriate as the first-order reference in the frequency range applied to correlograms. Whether or not the coda-correlation wavefield can be used to invert for the 1D structure of the Earth independently from travel time information observed in the seismic wavefield, remains to be determined.

3.5. Numerical simulation of earthquake coda

Synthetic computations of earthquake coda in a spherically-symmetric Earth model involve a synthesis of seismic waveforms a number of hours after the origin time, which can be computationally challenging. However, given recent advancements in computational seismology, the synthetic experiments should accompany interpretations in global-correlation studies as is the case in the traditional seismology.

In one of the pioneering studies on global interferometry, Ruigrok et al. (2008) presented a numerical simulation by means of a staggered-grid finite-difference method in an acoustic disk. Boué et al. (2014) used an early version of the axisymmetric spectral-element method (AxiSEM) (Nissen-Meyer et al., 2008) to generate 2-day-long synthetic seismograms. The results presented the first dependable comparison of the observed and synthetic correlograms despite a relatively modest quality of the synthetic correlogram. Wu et al. (2018) were successful in utilising the Direct Solution Method (DSM – Kawai et al., 2006) to generate several-hour-long seismograms to verify the feasibility of extracting inner-core sensitive phases in a 1D Earth model. In the DSM

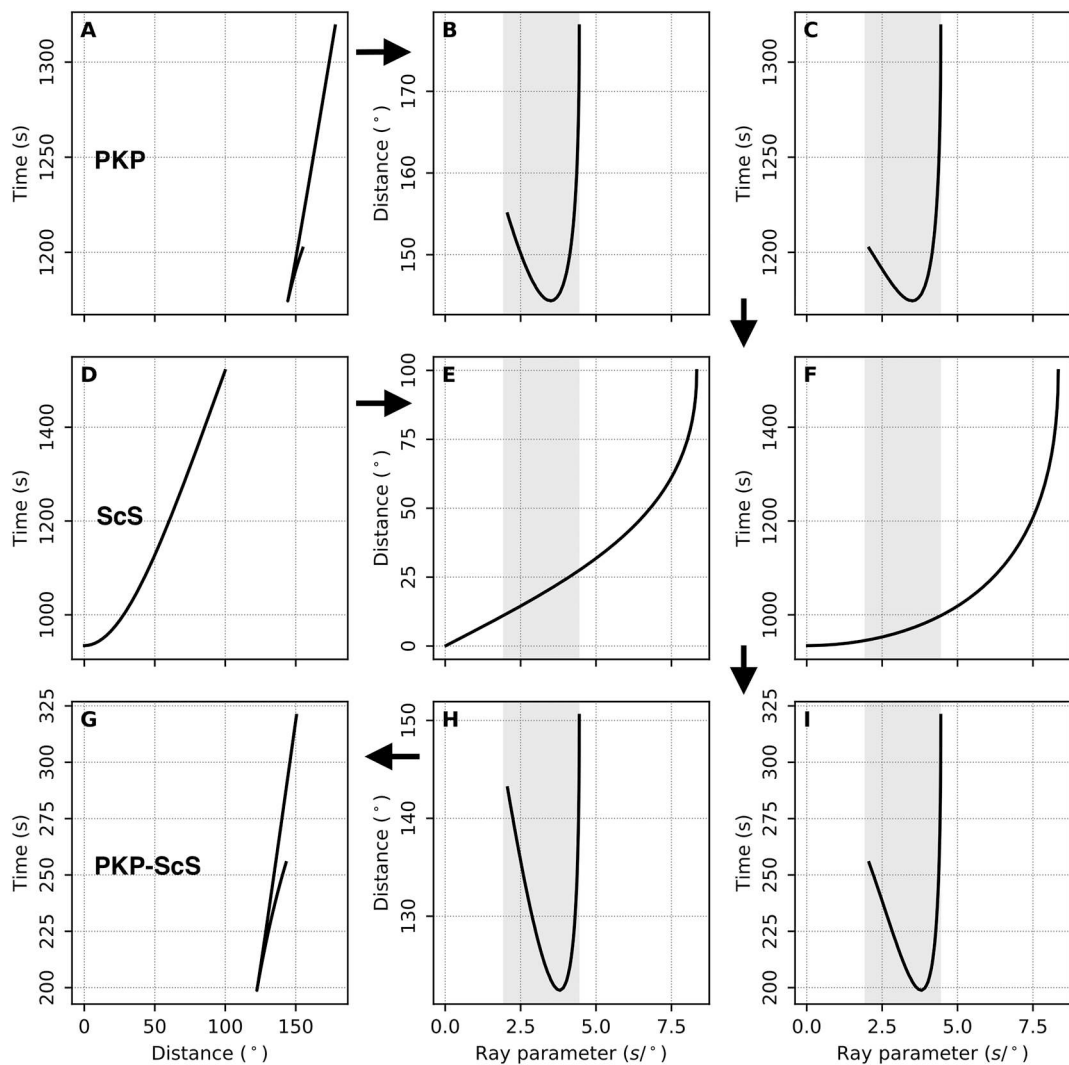


Fig. 15. Derivation of the travel time curve of the correlated phase PKP-ScS. (A) A normal travel time curve of PKP phase as a function of epicentral distance. (B) Epicentral distance and (C) travel time as functions of ray parameters for the core phase. (D), (E) and (F) are similar to (A), (B) and (C) but for ScS phase. (G) Differential travel time (blue) of the correlation feature PKP-ScS as a function of differential epicentral (or inter-receiver) distance (obtained from steps in panels H and I). This is the prediction travel time curve for the differential correlation phase. (H) Differential travel time and (I) differential epicentral distance (or inter-receiver distance) of PKP and ScS deducted from (B, C) and (E, F) as functions of ray parameters. All plotted curves are computed by the TauP toolkit (Crotwell et al., 1999) for a source at depth 0 km in the reference model ak135 (Kennett et al., 1995). The arrows indicate the chronological steps of the procedure. (For interpretation of the references to color in this figure legend, the reader is referred to the web version of this article.)

method, each simulation generates a seismogram for a pair of event and station in a separate run. Thus, the simulation has to be repeated many times for a single Earth input model for each individual seismogram and this can be a tedious task if there are many stations and events involved.

A recent advancement in computational seismology includes the development of a parallel spectral element method AxiSEM (Nissen-Meyer et al., 2014; van Driel et al., 2015; van Driel and Nissen-Meyer, 2014a, 2014b) to simulate 3D wavefield propagation in a 1D spherical symmetric Earth model (2.5-dimensional wavefield). This community-code for global wavefield simulation was benchmarked for its performance in terms of numerical stability as well as the stability in high-performance computing clusters. Another advantage of the AxiSEM method is that the entire wavefield can be saved after each model run. Thus, one can generate multiple seismograms of different source-receiver locations with a trivial computational cost added for the same Earth model. This is a helpful property because it enables to investigate

the reconstruction of the correlation wavefield for a realistic source-receiver configuration. Pham et al. (2018) obtained a strikingly similar synthetic and observed correlograms using the ak135f model (Kennett et al., 1995; Montagner and Kennett, 1996). This provided an independent validation of a widely-used 1D Earth models. Moreover, Tkalčić and Pham (2018) exploited the flexibility of AxiSEM to vary the input Earth models and identify the correlation features directly sensitive to the shear properties in the Earth's inner core (see Section 4 for more details). AxiSEM was also used to demonstrate the potential of the autocorrelation wavefield for probing the Europa's interior (Panning et al., 2018).

4. Applications

In comparison with the correlation methods that are used to reconstruct the surface waves between pairs of receivers, the applications

involving body waves responsible for the correlogram features are still in their infancy. Most studies have so far focused on the discovery of the signals that are related to Earth structure and efforts in understanding their formation mechanism. Here, we review recent attempts to utilise the body-wave contributions to the correlogram features to study Earth structure at the global scale, and we refer to Nakata et al. (2019) for reviews of applications at local and regional scales.

At the global scale, most studies focus on the Earth's inner core, although there were a couple of exceptions that focused on the lowermost mantle and the slab structure using "reconstructed" Green's functions from ambient noise (Poli et al., 2015; Spica et al., 2017). It is important to understand that the sensitivity to the inner core is a natural property of the correlation wavefield, where many prominent features stem from multiple reverberations from the Earth's internal discontinuities and steeply-incoming body waves that traverse the inner core and arrive at pairs of receivers with similar slowness. This is only convenient because the inner core has been poorly sampled by traveltime datasets of inner core-sensitive seismic phases. However, future studies related to Earth structure will most certainly not focus exclusively on the inner core, and it is just a question of time until the coda correlation wavefield will be harnessed to study other parts of the Earth.

4.1. Attempts to study P-wave properties of Earth's inner core

Seismological tools including body-wave and normal-mode analyses have provided significant knowledge of the Earth's inner core, yet much remains unresolved (Tkalcic, 2015, 2017). PKP waves are compressional body waves traversing the inner core at high frequencies (most dominant between 0.5 and 2 Hz) and provide significant level of detail on radial and lateral variation of the IC structures. Because the core is a geometric shadow zone for their propagation, they appear in three main branches: PKP_{df} (or PKIKP), PKP_{bc} and PKP_{ab}, as well as the reflected waves from the IC, PKiKP and the core boundaries-diffracted branches. However, the volumetric sampling of PKP waves is strongly confined due to uneven distribution of large earthquakes that efficiently radiate PKP waves at subduction zones, and receivers, mainly deployed on continents. Absolute time measurements of PKP waves are often subjected to a large uncertainty due to source location errors and crustal and mantle heterogeneity.

To obtain high-quality measurements, in which these mentioned obstacles can be somewhat mitigated, researchers have employed

differential-travel-time measurements of phase pairs with similar ray paths (e.g., Cormier and Choy, 1986; Sylvander and Souriau, 1996; Tanaka and Hamaguchi, 1997). In addition, it was recognized that the lowermost mantle, due to its strong heterogeneity, significantly perturbs the travel times of PKP_{ab} waves, and thus limits the use of ray-path pairs for studying the inner core to PKP_{bc}-PKIKP (Bréger et al., 2000; Romanowicz et al., 2003; Tkalcic et al., 2002). This extends the sensitivity range down to the depths of about 400 km beneath the inner-core boundary. Complementary PKIKP-PKiKP differential travel time dataset is suitable to study the very top of the inner core down to the depths of 80 km (e.g., Wen and Niu, 2002). Absolute travel times of PKIKP waves is a dataset that can still be used to probe down to the Earth's centre (e.g., Frost and Romanowicz, 2019; Ishii et al., 2002) and can be, arguably (Tkalcic, 2015), as reliable a tool as differential travel times if mantle structure can be adequately accounted for. Normal modes sensitive to inner core can also be exploited (Deuss, 2014), although, due to their long periods, they are appropriate to study general characteristics of the inner core and less likely to contribute to illuminating details on shorter spatial scales. In conclusion, the current coverage of the inner core with body waves is far from perfect, and largely confined to the upper layers of the inner core.

The great potential of the correlated body-wave signals to study the Earth's inner core through global correlation-stacks was recognized early (e.g., Boué et al., 2013; Lin et al., 2013; Lin and Tsai, 2013). Attempts to make practical uses of the extracted phases to study the compressional-wave structure of the Earth's inner core followed a few years later (Huang et al., 2015; Wang et al., 2015; Wang and Song, 2018). These early attempts, however, were made without a complete understanding of fine details of the formation of the correlogram features from both the theoretical (Pham et al., 2018; Poli et al., 2017) and the observational point of view (Wang and Tkalcic, 2020a, 2020b). Therefore, the theory errors propagated into attempts to link observations to Earth structure. In the following, we briefly summarize several of those past attempts at inferring Earth structure from global correlograms, and we review recent advances in studying the inner core by utilising core-sensitive correlation features.

Most of the previous studies utilised local, dense seismic networks, and in particular, a pair of prominent correlation features that have timing properties similar to the seismic phases PKIKPPKIKP and PKIIPKPPKIIKP, abbreviated as I2 and II2 (Fig. 16A). These correlation features (Fig. 16B) were interpreted to be related to the empirical Green's function (Earth's response) between multiple pairs of recording sites

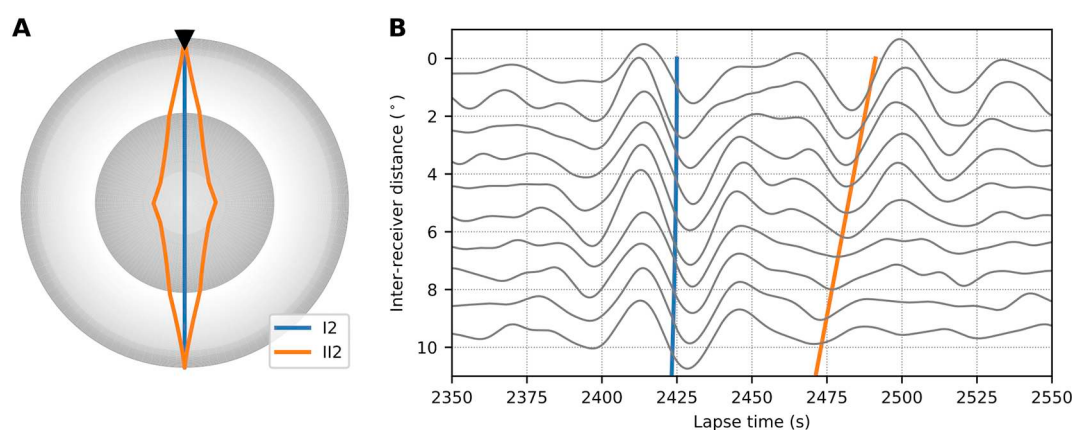


Fig. 16. a) Ray path of I2 and II2 waves. b) Correlation waveforms extracted from correlogram, the blue and orange lines denotes theoretical traveltimes for I2 and II2 given the reference model ak135. (For interpretation of the references to color in this figure legend, the reader is referred to the web version of this article.)

(e.g. Huang et al., 2015; Wang et al., 2015). In other words, according to that interpretation, travel times of the global correlogram features I2* and II2* were associated with the ray paths of the seismic phases I2 and II2 calculated from the receiver locations. Had the Green's function interpretation been correct, the observed data would have indeed provided valuable constraints on the centre of the inner core. As we stated earlier, because of a relative proximity of the I2 and II2 ray paths in the mantle (Fig. 16A), significant effects of mantle heterogeneity would have been mitigated. In addition, new geometries of deep Earth sampling would have been introduced due to the difference between the receiver-receiver configurations achieved here and source-receiver configurations in the mainstream seismological studies.

Wang et al. (2015) collected a differential travel time dataset interpreted as being II2-I2, (whereas we have in the meantime demonstrated that those were differential travel time measurements for the features II2* and I2*). This was done for 52 dense seismic networks over the globe. The network distribution near the equator was then improved in Wang and Song (2018). Their measurements and the subsequent interpretation invoked the existence of an innermost inner core (IMIC) with its fast axis tilted near the equator beneath South America. Although the details of anisotropy are different, the existence of IMIC is in agreement with some previous findings (e.g., Ishii and Dziewoński, 2002). At the same time, they are at odds with the inference from a global data set of PKIKP absolute travel time data (Frost and Romanowicz, 2019; Romanowicz et al., 2016) and numerous differential travel time studies summarised in Tkalcic (2017).

Huang et al. (2015) collected a differential travel time dataset of the same phases as above, but using a large number of recordings by the dense, USArray, network. That study led to an interpretation of results and inference in conjunction with hemispherical structure at the top of the Earth's inner core, also invoked in previous studies (e.g., Tanaka and Hamaguchi, 1997). The obtained geographical location of the boundary was at odds with previous findings (e.g., Waszek and Deuss, 2011).

In the most recent study, Wang and Tkalcic (2020a, 2020b) demonstrated through direct observations taking the correlogram feature I2* as an example, that it is made up of many body-wave cross-terms rather than representing the so called reconstructed seismic body-wave phase. The contribution of various constituents to the correlogram features strongly varies among differently chosen source locations and the used coda window relative to the correlation origin time (Wang and Tkalcic, 2020b). Therefore, if a careful selection of sources and receivers is not made prior to stacking, this will result in significant variations in the phase and travel times of the correlated features I2* and II2*. In turn, this will lead to erroneous interpretations.

4.2. S-wave properties of Earth's inner core by from the coda-correlation wavefield

The solidity of the Earth's inner core was proposed by Birch (1940) soon after its discovery by Lehmann (1936). The analysis of normal-mode data (Dziewoński and Gilbert, 1971) provided evidence for the solidity of the IC and was used to estimate the S-wave speed and attenuation profile in the inner core. It was recognized that the detection of inner-core shear waves would have provided crucial evidence backing up the solidity of the Earth's inner core at higher resolution. The direct shear-wave phase in the inner core is PKJKP, and thus a direct evidence of the inner core solidity would come through a detection of PKJKP waves or their surface reflections such as SPKJKP or PPKJKP (for the full list of references, see a review in Tkalcic and Pham (2018)).

However, that detection of PKJKP waves has been challenging due to weak amplitudes that shear waves in the inner core should theoretically have due to the conversions of energy from P-to-S and S-to-P waves at the inner-outer core boundary. Thus, the observation of the PKJKP was considered to be the "Holy Grail of Body Wave Seismology" (Shearer, 2009). Although there were few claims of detection of PKJKP, Shearer et al. (2011) suggested that those previous long-period observations were probably results of scatterings or special focusing effects.

Tkalcic and Pham (2018) abandoned a conventional search for PKJKP waves approach and employed recent insights into the formation of the correlogram features. The signals that were sensitive to the propagation of shear waves through the Earth's inner core (PKJKP) were found in the correlation pair with the compressional inner-core wave, I2. The existence of shear-wave sensitive features was then confirmed through a series of synthetic experiments, in which the shear-wave speed in the bulk of the IC was varied in a parameter search fashion. The experiment detected the variation of the correlation feature formed as I2-PKJKP that changes in a predicted manner given the input IC model (Fig. 17).

Shear-wave speed in the IC is reduced 2.5% with respect to the value reported in PREM. Such low shear-wave speed could be potentially explained by the presence of light elements in the iron-alloys at the inner-core conditions (Lai et al., 2020). The diffusion of body-centred cubic phase of iron atoms in solid state has also been proposed to explain low shear modulus (Belonosko et al., 2017). However, this reduction does not appear to be supported by a normal modes study (Robson and Romanowicz, 2019). The discrepancy could possibly be due to the dispersion of S wave speeds of inner-core materials or fixed density in the reference model. The frequency content of the correlogram features is in the period range 15–50 s, while the periods of the normal-mode data generally exceed 100 s. There is also a possibility to constrain shear-attenuation properties in the IC using the amplitude information contained in the correlogram features as initially experimented by Tkalcic and Pham (2018). However, further investigation is needed to reach a conclusive outcome since the amplitudes in the correlation wavefield are yet to be fully understood.

4.3. Towards coda correlation tomography

It has been shown recently that coda-correlation can be used to constrain Earth structure through a tomography framework (Wang and Tkalcic, 2020a). To construct the correlogram data-Earth structure relationship, it was shown that coda-correlogram features are decomposed into constituents, and an individual constituent is as a cross-term between two seismic waves. In a simplified treatment, the sensitivities of the two seismic waves to Earth structure were determined in the high-frequency approximation. For example, based on the time-measurements and ray theory, the relationship between a coda-correlation constituent and Earth structure is:

$$t_{ij}(\mathbf{m}; \mathbf{x}_s, \mathbf{x}_{r1}, \mathbf{x}_{r2}) = \int_{\text{path}_i(\mathbf{x}_s, \mathbf{x}_{r1})} \mathbf{mdl} - \int_{\text{path}_j(\mathbf{x}_s, \mathbf{x}_{r2})} \mathbf{mdl}, \quad (17)$$

where t_{ij} is the time measurement of a constituent of a specific correlogram feature, that is the cross-term between the i th and the j th seismic waves. The two seismic waves sample Earth structure, parameterized as model $\mathbf{m} = \left\{ \frac{1}{v} \right\}$ in which v denotes the seismic wave velocity, along the ray-paths, path_i and path_j . The ray-paths can be determined given the locations of the source event, \mathbf{x}_s and the two receivers, \mathbf{x}_{r1} and \mathbf{x}_{r2} . For example, Fig. 5 shows the ray-paths of cross-

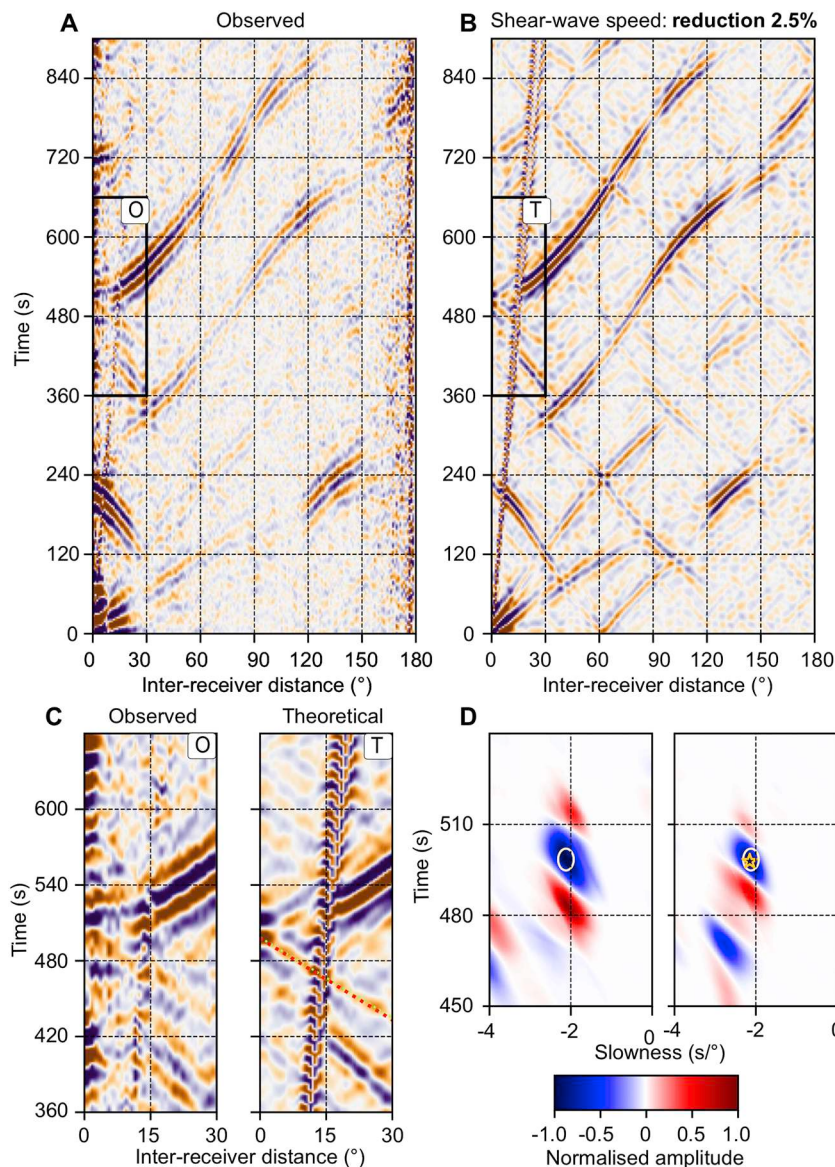


Fig. 17. Observed and synthetic correlograms and the I2-PKJKP cusp. (A and B) A comparison between (A) the observed global correlogram and (B) the best-fit simulated global correlogram for the central period of 23.1 s. The best-fit simulation uses the PREM model with shear-wave speed in the bulk of the inner core reduced by 2.5% [we used a smooth parameter-space search, best viewed as an animation (14)]. Compare with the cusp positions in Fig. 2. (C) Enlargements of windows O (observed) and T (theoretical) in (A) and (B), focused on the I2-PKJKP cusp. (D) The observed and simulated (theoretical) slant stacks. The yellow circle corresponds to the lower branch of the I2-PKJKP cusp in the slowness-time domain, and the yellow dotted line corresponds to the same in the travel-time domain. The red star in (D) and red dotted line in (C) are the values based on the best-fit Earth model with the 2.5% reduction of shear-wave speed in the inner core. Adopted from Tkalčić and Pham (2018). (For interpretation of the references to color in this figure legend, the reader is referred to the web version of this article.)

terms that are I2* constituents.

Eq. (17) has the form of $t_{ij} = g_{ij}(\mathbf{m})$, where g_{ij} denotes the tomographic relationship between the time t_{ij} of a coda-correlation constituent and Earth structure model \mathbf{m} . The relationship can be built for each of the coda correlogram-feature constituents, and a tomography problem can be posed:

$$\begin{pmatrix} t_{00} \\ t_{01} \\ \vdots \\ t_{ij} \\ \vdots \end{pmatrix} = \begin{pmatrix} g_{00}(\mathbf{m}) \\ g_{01}(\mathbf{m}) \\ \vdots \\ g_{ij}(\mathbf{m}) \\ \vdots \end{pmatrix}. \quad (18)$$

Eq. (18) is in the form of an inverse problem $\mathbf{G}(\mathbf{m}) = \mathbf{d}$, where $\mathbf{G} = \{g_{ij}\}$ represents the tomography kernel for Earth structure model \mathbf{m} and data $\mathbf{d} = [t_{00}, t_{01}, \dots, t_{ij}, \dots]^T$.

The location of the seismic event is an important parameter in the coda-correlation tomography (Wang and Tkalčić, 2020b). As shown in Eq. (17), the tomographic kernel, based on the $path_i$ and $path_j$,

significantly depends on the location of the event, although the stacked correlograms do not show the dependency on event locations, and the features seem invariable in the scale of hours (Fig. 13). This is fundamentally different from the conventional approach that treats the extracted signals as part of a structural Green's function, in which source locations are ignored. For example, as shown in Fig. 18, the synthetic model cannot be recovered if the coda-correlation feature I2* is treated as a “reconstructed” seismic wave, I2. In comparison, the model recovery is remarkably improved when the ray-path geometry of the main constituents is considered based on Eq. (17).

The tomographic relationship based on ray-theory (Eq. (1)) can be extended with finite-frequency methods (e.g., Dahlen et al., 2000; Hung et al., 2000; Marquering et al., 1999). Finite-frequency approaches would better match coda-correlation tomography because the correlation features are prominent at intermediate periods. The finite-frequency relationship would be similar to Eq. (17) that uses cross-terms between seismic waves to relate coda-correlation features to Earth structure.

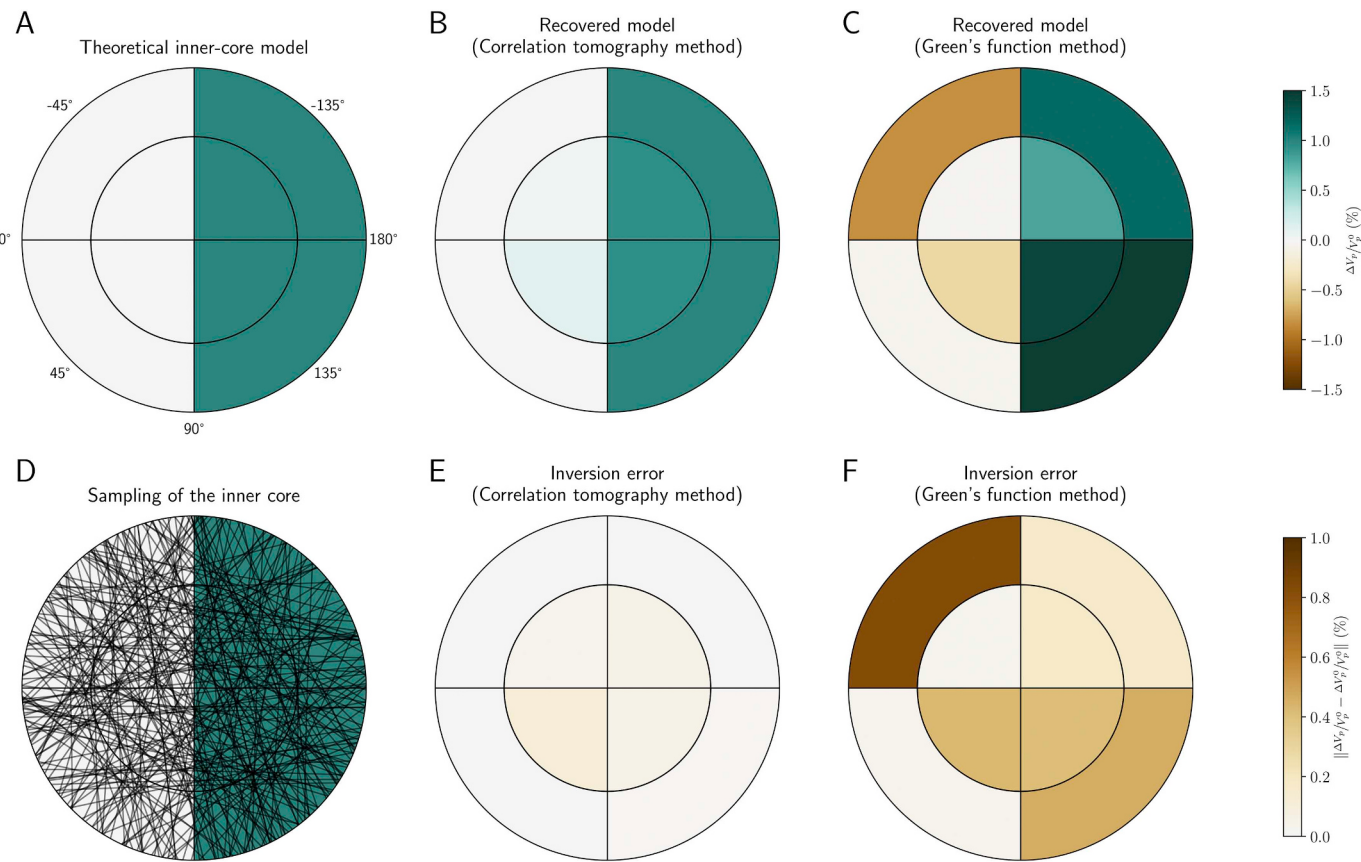


Fig. 18. Tomography results for the toy problem. (a) Theoretical P wave velocity perturbations in the inner core and the parameterization scheme dividing the inner core into eight equal pieces. (b-c) Recovered models using the new method and Green's function method, respectively. (d-e) Inversion errors for two approaches, respectively. Adopted from Wang and Tkalčić (2020a).

5. Concluding remarks

We presented a comprehensive review of theoretical and methodological developments of the coda-correlation as well as the applications to studying the Earth's deep structure. The main conclusions are as follows.

- (1) There is a fundamental difference between the cross-correlation of ambient-noise wavefield and the cross-correlation of late earthquake-coda wavefield. In the former, energy near Earth's surface is much more equally distributed in different directions, and spurious arrivals on individual cross-correlation functions are likely to destructively interfere and cancel each other – hence ambient noise cross-correlation stacks converge to reconstructed surface waves. In the latter, cross-correlation functions are dominated by cross-terms of reverberating body-waves that arrive at the given pair of receivers with the same slowness complying with the stationary-phase principle. These are fundamentally different from “reconstructed” body-wave parts of the structural Green's functions.
- (2) The features in the late earthquake-coda correlograms are dominated by the cross-terms between seismic phases sensitive to the deep-Earth structure that propagate in the great-circle plane mostly from reverberations between the Earth's free surface and the core-mantle boundary, whereas the interactions with minor discontinuities and lateral heterogeneity are insignificant. The similarity in the waveforms that contribute to the prominence of the

cross-correlation peaks of the correlogram features follows from the stationarity principle. However, the contributions of phases from the near-stationary points are prevalent in all observed correlogram features, which is evident from the fact that global earthquake sources are almost never located exactly in the stationary points for a given pair of receivers.

- (3) The correlogram features can be decomposed into separate constituents, and their relationship with Earth structure can be established using ray theory. There are numerous constituents of a single correlogram feature and it is possible to utilise “exotic” seismic phases that have not yet been observed in conventional seismology. Including more constituents in seismic tomography has the potential to decrease the singularity of the inverse problem, and improve the reliability of the tomographic inversion and our capacity to infer deep Earth structure.
- (4) Coda-correlation processing shares many similar components with ambient-noise processing. The prominence of the features in global coda-correlogram is a function of the input data selection: the specific portion of earthquake coda (the selection of the coda window), the earthquake magnitude and the earthquake mechanisms.
- (5) Future applications include but are not limited to studying the compressional- and shear-wave structure of the inner core, global tomography including both the cores and the mantle, and last but not least, studies of the planetary interiors in the future planetary missions.

Declaration of competing interest

None.

Acknowledgments

We acknowledge useful discussions with the members of the Seismology & Mathematical Geophysics group at Research School of Earth Sciences. We are grateful to two anonymous reviewers for their invaluable suggestions that helped improve the manuscript. Some calculations were performed on the Terrawulf cluster, a computational facility supported through the AuScope Australian Geophysical Observing System (AGOS). Other computations were completed using

the National Computational Facility under the ANU allocation scheme and the current grant: "Studying the Earth's interior using global correlation wavefield". The waveform data used to construct global correlograms are downloaded from IRIS Data Management Center. The facilities of IRIS Data Services, and specifically the IRIS Data Management Center, were used for access to waveforms, related metadata, and/or derived products used in this study. IRIS Data Services are funded through the Seismological Facilities for the Advancement of Geoscience (SAGE) Award of the National Science Foundation under Cooperative Support Agreement EAR-1851048. Finally, we would like to acknowledge the contributions of workers on this subject who have influenced this paper even if they might feel that their views are not fully represented.

Appendix A. Glossary of selected terms

Ambient-noise wavefield – a continuing, background ground motion due to the interaction of the solid earth with the oceans and atmosphere and other anthropogenic and natural sources.

Autocorrelation – the cross-correlation of a time series with itself (see *cross-correlation*).

Coda – seismic waves that exist due to scattering of seismic wavefield in the earth and are recorded a long time after the origin time of earthquakes and the passage of direct source-receiver propagation waves.

Correlogram – a two-dimensional graphical representation of stacked cross-correlation functions in inter-receiver angular-distance bins.

Correlation wavefield – a term coined to represent an abstract wavefield resulting from cross-correlation of seismograms from the regular seismic wavefield.

Correlation features – visible prominent and less prominent signals that are coherently seen over a range of distances in the correlogram, often resembling travel-time curves of specific seismic phases in the seismic sections. Regarding the nomenclature of a correlation feature, if the feature has similar timing property with a regular seismic phase, we use the standard nomenclature of that seismic phase with an asterisk. For example, the correlation feature PcP^* is a result of the maxima in the correlation functions generated by the waveform similarity among body waves involving PcP . Otherwise, a correlation feature is named by a differential naming convention of two involving phases. For example, $cS-cP$ refers to a prominent correlation feature that has no equivalence in the seismic wavefield.

Cross-correlation – a process of measuring similarity between two time series (of ground displacement, velocity or acceleration seismograms in our context) as a function of the time displacement of one time series relative to the other.

Cross-correlation function – a function in which cross-correlation, typically normalised between -1 and 1, is associated with the time displacement between the two input time series to which cross-correlation is applied.

Cross-correlation stack - a stack (sum) of a set of cross-correlation functions, e.g. for a single receiver pair over many events, or for many receiver-pairs within the same inter-receiver angular-distance bin.

Seismic phases – surface a body waves recorded on seismograms and denoted by different symbols depending on the geometry of their source-receiver paths through the Earth. For example, the phase PcP stands for body waves that travel from the source as P waves (P), reflect from the Earth's core (c) and travel to a receiver also as P waves (P).

Seismic wavefield – a volume taken up by seismic waves that propagate from a seismic source that is manifested as a ground motion time series recorded at a receiver.

Appendix B. Building of coda-correlogram in the programming language Python

We provide a commented program in Python that performs pre-processing and processing steps from raw seismograms (in SAC format) for a selected event. It then computes event-coda correlation stack and plots it according to the procedure described in [Section 3](#) (Methods). Most libraries used in the program are built-in: *number*, *glob*, *os*, *time*, *multiprocessing*, *threading*, *warnings*. Additionally, users might need to install the following packages: *obspy*, *pyfftw*, *netcdf4*. The links to these packages are provided here:

<https://github.com/obspy/obspy/wiki>

<https://pypi.org/project/pyFFTW/>

<http://unidata.github.io/netcdf4-python/netCDF4/index.html>

For new Python users, we encourage the use of Anaconda (<https://www.anaconda.com>) to manage their software packages. Once Anaconda is installed, the above packages can be installed by executing the following command in their terminal:

```
conda install obspy pyfftw netcdf4
```

Finally, *libgcc* contains important supporting functions and is included in this package.

Jupyter notebook including the associated library and example data can be publicly accessed at https://github.com/tsonpham/ESR_CorrelationWavefield.git.

Import necessary libraries

```
## Build-in libraries
import multiprocessing as mp
import threading
import numpy as np
import os
import time
import warnings
from obspy import UTCDateTime
from obspy.geodetics import locations2degrees

## Supporting functions for global cross-correlation
import libgcc
```

Pre-determined parameters

```
## Coda time window from the event origin time (in seconds)
window_start, window_end = 10000, 35000

## Temporal normalization parameters
# Pre-filter period band used in the computation of the normalization
# weight
ram_fband = (0.02, 0.067) # seconds
# Window width of the running absolute-mean temporal normalization
temp_width = 128 # seconds

## Spectral normalization parameter: width of the normalization
spec_width = 2e-3 # Hz

## Number of parallel processors used in parallel
nprocs = 4

## Pre-determined size of inter-receiver bin
bin_size = 1 # degrees

## Directory of merged waveforms
path_name = 'Data/Event_2017.01.22.04.30.22.990'
```

1. Read coda waveforms

```
## Wildcast of the waveform file names
wildcast = os.path.join(path_name, '*.SAC')
## String determine the event origin time
eventstr = os.path.basename(path_name)
## Get origin time from the eventstr
origintime = UTCDateTime().strptime(eventstr, 'Event_%Y.%m.%d.%H.%M.%S.%f')

start = time.time()
data_stream = libgcc.ReadData(wildcast, origintime, window_start,
window_end-window_start)
end = time.time()
delta = data_stream[0].stats.delta
ntraces = len(data_stream)

print ('Read in coda waveform')
print ('> Coda time window: %d - %d s after the origin time' % \
(window_start, window_end))
print ('> Sampling rate: %.2f sps' % (1 / delta))
print ('> Number of seismograms: %d' % ntraces)
print ('> Reading time: %.2f s\n' % (end-start))
```

2. Initialize pre-processors

```
#### Initialization of GCC processors

## Number of waveform points pre-determined from window range and sampling
time delta
npts = int(np.round((window_end - window_start) / delta))
## Number of points in the FFT transform traces, which is double
fft_npts = 2 * npts
## Initialization
start = time.time()
xcc = list()
for ii in range(nprocs):
    xcc.append(libgcc.GCC(fft_npts, temp_width, spec_width, ram_fband))
end = time.time()

print ('Initializing %d GCC processors:' % nprocs)
print ('> npts:', npts)
print ('> fft npts:', fft_npts)
print ('> Temporal normalization - width: %.1f s' % temp_width)
print ('                                - weight bandpass: %.3f - %.3f Hz' % ram_fband)
print ('> Spectral normalization (whitening): %.1f mHz' % (spec_width * 1e3))
print ('> Initializing time: %.3f s\n' % (end-start))
```

3. Perform single-station waveform pre-processing

```
#### Preprocessing of single-station waveforms that include temporal and
spectral normalization
def pre_proc(my_xcc, my_stream, my_indices, output_real, output_imag):
    spec_npts = my_xcc.get_spec_npts()
    for ii, tr in zip(my_indices, my_stream):
        try:
            # pre-process job
            with warnings.catch_warnings():
                warnings.simplefilter("ignore")
                spec = my_xcc.pre_proc(tr)
            # assign to global data
            if np.all(np.isfinite(spec)):
                output_real[ii*spec_npts:(ii+1)*spec_npts] = np.real(spec)
                output_imag[ii*spec_npts:(ii+1)*spec_npts] = np.imag(spec)
        except Exception as ex:
            pass #print (ex)

#### Preprocessing of waveform data ####
## Declare a common memory block to be shared by different processors.
## Pre-processed spectral traces are stored in the memory block array.
spec_real = mp.Array('f', ntraces*xcc[0].get_spec_npts(), lock=False)
spec_imag = mp.Array('f', ntraces*xcc[0].get_spec_npts(), lock=False)

## Preprocessing in parallel at multiple processors
## Results are stored in the shared memory block
print ('Pre-processing with %d workers' % nprocs)
start = time.time()
jobs = list()
```

```

for ii in range(nprocs):
    my_indices = np.arange(ii, ntraces, nprocs)
    p = mp.Process(target=pre_proc,
                   args=(xcc[ii], data_stream[ii:ntraces:nprocs], my_indices,
                         spec_real, spec_imag))
    p.start()
    jobs.append(p)
for p in jobs: p.join()
end = time.time()
## Converting the memory block (1D) in to 2D numpy array of complex
numbers.
spec_data = np.array(spec_real[:]) + np.array(spec_imag[:]) * 1j
spec_data = spec_data.reshape((ntraces, xcc[0].get_spec_npts()))
print ('> Runtime (multi-threading): %.2f s\n' % (end-start))

```

4. Pre-compute inter-receiver histogram

```

##### Based on latitudes and longitudes of the existing station
## pre-compute inter-receiver distance pairs
lats = [tr.stats.sac.stla for tr in data_stream]
lons = [tr.stats.sac.stlo for tr in data_stream]

print ('Computing station pairs:')
print ('> Interstation distance bin_size:', bin_size, 'deg')
## building look-up table for inter-station bins
nbins = int(180. / bin_size)
npairs = int((ntraces * (ntraces + 1)) / 2)
cc_pairs = np.zeros((npairs, 3), dtype=int)
pair_hist = np.zeros(nbins, dtype=int)
start = time.time()
count = 0
for s1 in range(ntraces):
    for s2 in range(s1, ntraces):
        gcarr = locations2degrees(lats[s1], lons[s1], lats[s2], lons[s2])
        nb = int(np.round(gcarr / bin_size))
        nb = (nbins - 1) if nb >= nbins else nb
        cc_pairs[count, :] = [s1, s2, nb]
        pair_hist[nb] += 1
        count += 1
end = time.time()
print ('> Number of pairs: %d' % npairs)
print ('> Runtime (serial): %.2f s\n' % (end-start))

```

5. Compute and stack cross-correlation in frequency domain

```

##### Compute and stack cross-correlation in frequency domain

def calc_spec_xcorr(my_pairs, spec_data, safe_lock, spec_stack):
    # local buffer of cross-correlogram
    local_spec_cc = np.zeros((nbins, spec_data.shape[1]),
                             dtype='complex64')
    # cross-correlating and stacking in spectral domain
    for ii in range(my_pairs.shape[0]):
        s1, s2, nb = my_pairs[ii, :]
        spec1 = spec_data[s1]
        spec2 = spec_data[s2]
        local_spec_cc[nb, :] += spec1 * np.conj(spec2)
    # stack to global buffer
    safe_lock.acquire()
    spec_stack += local_spec_cc
    safe_lock.release()

```

```

# global buffer of cross-correlogram
spec_stack = np.zeros((nbins, xcc[0].get_spec_npts()), dtype='complex64');
safe_lock = threading.Lock()
## multi-processing
print ('Cross-correlating with %d workers ...' % nprocs)
start = time.time()
jobs = []
for ii in range(nprocs):
    my_pairs = cc_pairs[ii:count:nprocs, :]
    p = threading.Thread(target=calc_spec_xcorr,
                          args=(my_pairs, spec_data, safe_lock, spec_stack))
    p.start()
    jobs.append(p)
for p in jobs: p.join()
end = time.time()
print ('> Runtime (multi-threading): %.2f s\n' % (end-start))

```

6. Inverse FFT of stacked frequency correlogram

```

#####
##### INVERSE FFT AND CREATE CC #####
# buffer for cross-correlogram in time domain
corrwf = np.zeros((nbins, npts), dtype='float32')
print ('Inverse FFT')
start = time.time()
for nb in range(nbins):
    spec = spec_stack[nb, :]
    cc = xcc[0].inv_rfft(spec)
    sym_cc = 0.5 * (cc + cc[::-1])
    corrwf[nb, :] = sym_cc[0:npts]
end = time.time()
print ('> Runtime (serial): %.2f s' % (end-start))

```

7. Plot correlogram

```

import matplotlib.pyplot as plt
import libgcc

xmin, xmax = 0, 180
xstep = 30
ymin, ymax = 0, 3600
ystep = 600
##### 01 READ IN CORRELOGRAM #####
nbins, npts = corrwf.shape
imag = libgcc.NormalizeFilter(corrwf.copy(), pair_hist, delta, 15, 50)

VMAX = 2e-2 * np.max(np.abs(imag))
# imag[imag>VMAX] = VMAX
# imag[imag<-VMAX] = -VMAX

##### 02 READ IN CORRELOGRAM #####
fig = plt.figure(figsize=(6.5, 10.5))
gs = fig.add_gridspec(5, 3)
ax = fig.add_subplot(gs[1:5, 0:2])
axHist = fig.add_subplot(gs[0, 0:2], sharex=ax)
axKey = fig.add_subplot(gs[0:5, 2], xticks=[], yticks=[], frameon=False)

```

```

##### 03 DISPLAY CORRELOGRAM #####
time_max = npts * delta
ax.imshow(imag.T, vmax=VMAX, vmin=-VMAX, aspect='auto', cmap='PuOr',
          extent=(0, 180, time_max, 0), interpolation='sinc')
ax.grid(ls='--', color='k', lw=0.5, alpha=0.5)
xticks = np.arange(xmin, xmax+1, xstep).astype(int)
ax.set_xticks(xticks)
ax.set_xlabel('Inter-receiver Distance ($^\circ$)')
yticks = np.arange(ymin, ymax+1, ystep).astype(int)
ax.set_yticks(yticks)
ax.set_xlim(ymin, ymax)
ax.set_ylabel('Time (s)')

##### 04 PLOT PREDICTION #####
if with_prediction:
    try:
        plot_prediction(ax, axKey, taup_curve_fname, prediction_fname,
                        linestyle)
    except Exception as ex:
        print (ex)

##### 04 PLOT HISTOGRAM #####
axHist.bar((np.arange(nbins)+0.5)*bin_size, pair_hist, width=1.0,
           color='gray')
axHist.set_ylabel('Number of\n correlation pairs')
axHist.set_xlim(xmin, xmax)
axHist.grid(ls=':', color='gray', lw=.5)

## Stretch layout and save figures
gs.tight_layout(figsize=fig)
plt.savefig('Output/EventCorrelogram.pdf')
plt.show()

```

References

- Belonoshko, A.B., Lukinov, T., Fu, J., Zhao, J., Davis, S., Simak, S.I., 2017. Stabilization of body-centred cubic iron under inner-core conditions. *Nat. Geosci.* 10, 312–316. <https://doi.org/10.1038/ngeo2892>.
- Bensen, G.D., Ritzwoller, M.H., Barmin, M.P., Levshin, A.L., Lin, F., Moschetti, M.P., Shapiro, N.M., Yang, Y., 2007. Processing seismic ambient noise data to obtain reliable broad-band surface wave dispersion measurements. *Geophys. J. Int.* 169, 1239–1260. <https://doi.org/10.1111/j.1365-246X.2007.03374.x>.
- Bensen, G.D., Ritzwoller, M.H., Shapiro, N.M., 2008. Broadband ambient noise surface wave tomography across the United States. *J. Geophys. Res.* 113. <https://doi.org/10.1029/2007JB005248>.
- Birch, A.F., 1940. The alpha-gamma transformation of iron at high pressures, and the problem of the earth's magnetism. *Am. J. Sci.* 238, 192–211.
- Bonnefoy-Claudet, S., Cotton, F., Bard, P.-Y., 2006. The nature of noise wavefield and its applications for site effects studies: a literature review. *Earth Sci. Rev.* 79, 205–227. <https://doi.org/10.1016/j.earscirev.2006.07.004>.
- Boschi, L., Weemstra, C., 2015. Stationary-phase integrals in the cross correlation of ambient noise. *Rev. Geophys.* 53, 411–451. <https://doi.org/10.1002/2014RG000455>.
- Boué, P., Poli, P., Campillo, M., Pedersen, H., Briand, X., Roux, P., 2013. Teleseismic correlations of ambient seismic noise for deep global imaging of the Earth. *Geophys. J. Int.* 194, 844–848.
- Boué, P., Poli, P., Campillo, M., Roux, P., 2014. Reverberations, coda waves and ambient noise: correlations at the global scale and retrieval of the deep phases. *Earth Planet. Sci. Lett.* 391, 137–145. <https://doi.org/10.1016/j.epsl.2014.01.047>.
- Bréger, L., Tkalcic, H., Romanowicz, B., 2000. The effect of D on PKP(AB-DF) travel time residuals and possible implications for inner core structure. *Earth Planet. Sci. Lett.* 175, 133–143.
- Brenguier, F., Campillo, M., Hadzioannou, C., Shapiro, N.M., Nadeau, R.M., Larose, E., 2008. Postseismic relaxation along the San Andreas fault at Parkfield from continuous seismological observations. *Science* 321, 1478–1481. <https://doi.org/10.1126/science.1160943>.
- Buland, R., Chapman, C.H., 1983. The Computation of Seismic Travel Times. *Bull. Seismol. Soc. Am.* 73, 1271–1302.
- Campillo, M., Paul, A., 2003. Long-range correlations in the diffuse seismic coda. *Science* 299, 547–549.
- Claerbout, J.F., 1968. Synthesis of a layered medium from its acoustic transmission response. *Geophysics* 33, 264–269. <https://doi.org/10.1190/1.1439927>.
- Cooley, J.W., Tukey, J.W., 1965. An algorithm for the machine calculation of complex Fourier series. *Math. Comput.* 19, 297–301. <https://doi.org/10.1090/S0025-5718-1965-0178586-1>.
- Cormier, V.F., Choy, G.L., 1986. A search for lateral heterogeneity in the inner core from differential travel times near PKP-D and PKP-C. *Geophys. Res. Lett.* 13, 1553–1556. <https://doi.org/10.1029/GL013i013p01553>.
- Crotwell, H.P., Owens, T.J., Ritsema, J., 1999. The TauP Toolkit: flexible seismic travel-time and ray-path utilities. *Seismol. Res. Lett.* 154–160.
- Dahlen, F.A., Hung, S.-H., Nolet, G., 2000. Fréchet kernels for finite-frequency traveltimes—I. Theory. *Geophys. J. Int.* 141, 157–174. <https://doi.org/10.1046/j.1365-246X.2000.00070.x>.
- Deuss, A., 2014. Heterogeneity and anisotropy of Earth's inner core. *Annu. Rev. Earth Planet. Sci.* 42, 103–126. <https://doi.org/10.1146/annurev-earth-060313-054658>.
- Dziewoński, A.M., Anderson, D.L., 1981. Preliminary reference Earth model. *Phys. Earth Planet. Inter.* 25, 297–356.
- Dziewoński, A.M., Gilbert, F., 1971. Solidity of the inner core of the Earth inferred from normal mode observations. *Nature* 234, 465–466. <https://doi.org/10.1038/234465a0>.
- Ekström, G., Nettles, M., Dziewoński, A.M., 2012. The global CMT project 2004–2010: centroid-moment tensors for 13,017 earthquakes. *Phys. Earth Planet. Inter.* 200–201, 1–9. <https://doi.org/10.1016/j.pepi.2012.04.002>.
- Fan, Y., Snieder, R., 2009. Required source distribution for interferometry of waves and diffusive fields. *Geophys. J. Int.* 179, 1232–1244. <https://doi.org/10.1111/j.1365-246X.2009.04358.x>.
- Fichtner, A., 2014. Source and processing effects on noise correlations. *Geophys. J. Int.* 197, 1527–1531. <https://doi.org/10.1093/gji/gju093>.
- Fichtner, A., Ermert, L., Gokhberg, A., 2017. Seismic noise correlation on heterogeneous supercomputers. *Seismol. Res. Lett.* 88, 1141–1145. <https://doi.org/10.1785/0220170043>.
- Forghani, F., Snieder, R., 2010. Underestimation of body waves and feasibility of surface-wave reconstruction by seismic interferometry. *Lead. Edge* 29, 790–794. <https://doi.org/10.1190/1.3462779>.
- Frost, D.A., Romanowicz, B., 2019. On the orientation of the fast and slow directions of anisotropy in the deep inner core. *Phys. Earth Planet. Inter.* 286, 101–110. <https://doi.org/10.1016/j.pepi.2018.11.006>.
- Galetti, E., Curtis, A., 2012. Generalised receiver functions and seismic interferometry. *Tectonophysics* 532, 1–26. <https://doi.org/10.1016/j.tecto.2011.12.004>.
- Huang, H.-H., Lin, F.-C., Tsai, V.C., Koper, K.D., 2015. High-resolution probing of inner core structure with seismic interferometry. *Geophys. Res. Lett.* 42, 10,622–10,630.
- Hung, S.-H., Dahlen, F.A., Nolet, G., 2000. Fréchet kernels for finite-frequency

- traveltimeseII. Examples. *Geophys. J. Int.* 141, 175–203. <https://doi.org/10.1046/j.1365-246X.2000.00072.x>.
- Ishii, M., Dziewoński, A.M., 2002. The innermost inner core of the Earth: evidence for a change in anisotropic behavior at the radius of about 300 km. *Proc. Natl. Acad. Sci.* 99, 14026–14030.
- Ishii, M., Tromp, J., Dziewoński, A.M., Ekström, G., 2002. Joint inversion of normal mode and body wave data for inner core anisotropy 1. Laterally homogeneous anisotropy. *J. Geophys. Res. Solid Earth* 107. <https://doi.org/10.1029/2001JB000712>. ESE 20–1–ESE 20–16.
- Kawai, K., Takeuchi, N., Geller, R.J., 2006. Complete synthetic seismograms up to 2 Hz for transversely isotropic spherically symmetric media. *Geophys. J. Int.* 164, 411–424. <https://doi.org/10.1111/j.1365-246X.2005.02829.x>.
- Kennett, B.L.N., Pham, T.-S., 2018b. Evolution of the correlation wavefield extracted from seismic event coda. *Phys. Earth Planet. Inter.* 282, 100–109. <https://doi.org/10.1016/j.pepi.2018.07.004>.
- Kennett, B.L.N., Pham, T.-S., 2018a. The nature of Earth's correlation wavefield: late coda of large earthquakes. *Proc. Royal Soc. A Math. Phys. Eng. Sci.* 474, 20180082. <https://doi.org/10.1098/rspa.2018.0082>.
- Kennett, B.L.N., Engdahl, E.R., Buland, R., 1995. Constraints on seismic velocities in the Earth from traveltimes. *Geophys. J. Int.* 122, 108–124.
- Kobayashi, N., Nishida, K., 1998. Continuous excitation of planetary free oscillations by atmospheric disturbances. *Nature* 395, 357–360. <https://doi.org/10.1038/26427>.
- Krischer, L., Megies, T., Barsch, R., Beyreuther, M., Lerocq, T., Caudron, C., Wassermann, J., 2015. ObsPy: a bridge for seismology into the scientific Python ecosystem. *Comput. Sci. Disc.* 8, 014003. <https://doi.org/10.1088/1749-4699/8/1/014003>.
- Lai, X., Zhu, F., Liu, Y., Bi, W., Zhao, J., Alp, E.E., Hu, M.Y., Zhang, D., Tkachev, S., Manghnani, M.H., Prakapenka, V.B., Chen, B., 2020. Elastic and magnetic properties of Fe3P up to core pressures: phosphorus in the Earth's core. *Earth Planet. Sci. Lett.* 531, 115974. <https://doi.org/10.1016/j.epsl.2019.115974>.
- Lehmann, I., 1936. P. *Publ. Bur. Cent. Séismolog. Int.* A14 (3), S.87–115.
- Li, L., Boué, P., Campillo, M., 2020. Observation and explanation of spurious seismic signals emerging in teleseismic noise correlations in teleseismic noise correlations. *Solid Earth* 11, 173–184.
- Lin, F., Tsai, C.V., 2013. Seismic Interferometry with antipodal station pairs. *Geophys. Res. Lett.* 40, 4609–4613.
- Lin, F., Ritzwoller, M.H., Townend, J., Bannister, S., Savage, M.K., 2007. Ambient noise Rayleigh wave tomography of New Zealand. *Geophys. J. Int.* 170, 649–666.
- Lin, F.C., Moschetti, M.P., Ritzwoller, M.H., 2008. Surface wave tomography of the western United States from ambient seismic noise: Rayleigh and love wave phase velocity maps. *Geophys. J. Int.* 173, 281–298. <https://doi.org/10.1111/j.1365-246X.2008.03720.x>.
- Lin, F., Tsai, V.C., Schmandt, B., Duputel, Z., 2013. Extracting seismic core phases with array interferometry. *Geophys. Res. Lett.* 40, 1049–1053.
- Marquering, H., Dahmen, F.A., Nolet, G., 1999. Three-dimensional sensitivity kernels for finite-frequency traveltimes: the banana-doughnut paradox. *Geophys. J. Int.* 137, 805–815. <https://doi.org/10.1046/j.1365-246x.1999.00837.x>.
- Montagner, J.-P., Kennett, B.L.N., 1996. How to reconcile body-wave and normal-mode reference earth models. *Geophys. J. Int.* 125, 229–248. <https://doi.org/10.1111/j.1365-246X.1996.tb06548.x>.
- Moschetti, M.P., Ritzwoller, M.H., Shapiro, N.M., 2007. Surface wave tomography of the western United States from ambient seismic noise: Rayleigh wave group velocity maps. *Geochem. Geophys. Geosyst.* 8, 1–10. <https://doi.org/10.1029/2007GC001655>.
- Nakata, N., Gualtieri, L., Fichtner, A. (Eds.), 2019. Seismic Ambient Noise. Cambridge University Press, Cambridge; New York, NY. <https://doi.org/10.1017/9781082648080.010>.
- Nishida, K., 2013. Global propagation of body waves revealed by cross-correlation analysis of seismic hum. *Geophys. Res. Lett.* 40, 1691–1696.
- Nishida, K., Kobayashi, N., Fukao, Y., 2002. Origin of Earth's ground noise from 2 to 20 mHz. *Geophys. Res. Lett.* 29. <https://doi.org/10.1029/2001GL013862>. 52–1–52–4.
- Nissen-Meyer, T., Fournier, A., Dahmen, F.A., 2008. A 2-D spectral-element method for computing spherical-earth seismograms—II. Waves in solid-fluid media. *Geophys. J. Int.* 174, 873–888. <https://doi.org/10.1111/j.1365-246X.2008.03813.x>.
- Nissen-Meyer, T., van Driel, M., Stähler, S.C., Hosseini, K., Hempel, S., Auer, L., Colombi, A., Fournier, A., 2014. AXISEM: broadband 3-D seismic wavefields in axisymmetric media. *Solid Earth* 5, 425–445. <https://doi.org/10.5194/se-5-425-2014>.
- Panning, M.P., Stähler, S.C., Huang, H.-H., Vance, S.D., Kedar, S., Tsai, V.C., Pike, W.T., Lorenz, R.D., 2018. Expected seismicity and the seismic noise environment of Europa. *J. Geophys. Res.* 122. <https://doi.org/10.1002/2017JE005332>.
- Pedersen, H.A., Colombi, A., 2018. Body waves from a single source area observed in noise correlations at arrival times of reflections from the 410 discontinuity. *Geophys. J. Int.* 214, 1125–1135. <https://doi.org/10.1093/gji/ggy191>.
- Pham, T.-S., Tkalcic, H., 2017. On the feasibility and use of teleseismic P wave coda autocorrelation for mapping shallow seismic discontinuities. *J. Geophys. Res. Solid Earth* 122, 3776–3791. <https://doi.org/10.1002/2017JB013975>.
- Pham, T.-S., Tkalcic, H., 2018. Antarctic ice properties revealed from teleseismic P wave coda autocorrelation. *J. Geophys. Res. Solid Earth* 123, 7896–7912. <https://doi.org/10.1029/2018JB016115>.
- Pham, T.-S., Tkalcic, H., Sambridge, M., Kennett, B.L.N., 2018. Earth's correlation wavefield: late coda correlation. *Geophys. Res. Lett.* 45, 3035–3042. <https://doi.org/10.1002/2018GL077244>.
- Poli, P., Campillo, M., Pedersen, H., Group, L.W., 2012a. Body-wave imaging of Earth's mantle discontinuities from ambient seismic noise. *Science* 338, 1063–1065.
- Poli, P., Pedersen, H.A., Campillo, M., 2012b. Emergence of body waves from cross-correlation of short period seismic noise. *Geophys. J. Int.* 188, 549–558. <https://doi.org/10.1111/j.1365-246X.2011.05271.x>.
- Poli, P., Thomas, C., Campillo, M., Pedersen, H.A., 2015. Imaging the D reflector with noise correlations. *Geophys. Res. Lett.* 42. <https://doi.org/10.1002/2014GL062198>. 2014GL062198.
- Poli, P., Campillo, M., de Hoop, M.V., 2017. Analysis of intermediate period correlations of coda from deep earthquakes. *Earth Planet. Sci. Lett.* 477, 147–155.
- Rhie, J., Romanowicz, B., 2004. Excitation of Earth's continuous free oscillations by atmosphere-ocean-seafloor coupling. *Nature* 431, 552–556. <https://doi.org/10.1038/nature02942>.
- Robson, A.J.S., Romanowicz, B., 2019. New normal mode constraints on bulk inner core velocities and density. *Phys. Earth Planet. Inter.* 295, 106310. <https://doi.org/10.1016/j.pepi.2019.106310>.
- Romanowicz, B., Tkalcic, H., Bréger, L., 2003. On the origin of complexity in PKP travel time data. In: Earth's Core: Dynamics, Structure, Rotation. American Geophysical Union (AGU), pp. 31–44. <https://doi.org/10.1029/GD031p0031>.
- Romanowicz, B., Cao, A., Godwal, B., Wenk, R., Ventosa, S., Jeanloz, R., 2016. Seismic anisotropy in the Earth's innermost inner core: testing structural models against mineral physics predictions. *Geophys. Res. Lett.* 43, 93–100. <https://doi.org/10.1002/2015GL066734>.
- Ruigrok, E., Wapenaar, K., 2012. Global-Phase Seismic Interferometry Unveils P-Wave Reflectivity below the Himalayas and Tibet. *Geophys. Res. Lett.* 39. <https://doi.org/10.1029/2012GL051672>. L11303.
- Ruigrok, E., Draganov, D., Wapenaar, K., 2008. Global-scale seismic interferometry: theory and numerical examples. *Geophys. Prospect.* 56, 395–417.
- Ryberg, T., 2011. Body wave observations from cross-correlations of ambient seismic noise: a case study from the Karoo, RSA. *Geophys. Res. Lett.* 38. <https://doi.org/10.1029/2011GL047665>.
- Sager, K., Ermert, L., Boehm, C., Fichtner, A., 2018. Towards full waveform ambient noise inversion. *Geophys. J. Int.* 212, 566–590. <https://doi.org/10.1093/gji/ggx429>.
- Scherbaum, F., 1987. Seismic imaging of the site response using microearthquake recordings. Part I. Method. *Bull. Seismol. Soc. Am.* 77, 1905–1923.
- Sens-Schönfelder, C., Snieder, R., Stähler, S.C., 2015. The lack of equipartitioning in global body wave coda. *Geophys. Res. Lett.* 42. <https://doi.org/10.1002/2015GL065108>.
- Shapiro, N.M., Campillo, M., 2004. Emergence of broadband Rayleigh waves from correlations of the ambient seismic noise. *Geophys. Res. Lett.* 31. <https://doi.org/10.1029/2004GL019491>.
- Shapiro, N.M., Campillo, M., Stehly, L., Ritzwoller, M.H., 2005. High-resolution surface-wave tomography from ambient seismic noise. *Science* 307, 1615–1618.
- Shearer, P.M., 2009. Introduction to Seismology, 2nd ed. Cambridge University Press, University Printing House, Shaftesbury Road, Cambridge CB2 8BS, UK.
- Shearer, P.M., Rychert, C.A., Liu, Q., 2011. On the visibility of the inner-core shear wave phase PKJKP at long periods. *Geophys. J. Int.* 185, 1379–1383. <https://doi.org/10.1111/j.1365-246X.2011.05011.x>.
- Snieder, R., 2004. Extracting the Green's function from the correlation of coda waves: a derivation based on stationary phase. *Phys. Rev. E Stat. Phys. Plasmas Fluids Relat. Interdiscip. Topics* 69, 8. <https://doi.org/10.1103/PhysRevE.69.046610>.
- Snieder, R., Larose, E., 2013. Extracting Earth's elastic wave response from noise measurements. *Annu. Rev. Earth Planet. Sci.* 41, 183–206. <https://doi.org/10.1146/annurev-earth-050212-123936>.
- Spica, Z., Perton, M., Berroza, G.C., 2017. Lateral heterogeneity imaged by small-aperture ScS retrieval from the ambient seismic field. *Geophys. Res. Lett.* 44. <https://doi.org/10.1002/2017GL073230>.
- Stein, S., Wyssession, M., 2003. An Introduction to Seismology, Earthquakes, and Earth Structure. Blackwell Publishing Ltd, Oxford, UK.
- Sun, W., Kennett, B.L.N., 2016. Receiver structure from teleseisms: Autocorrelation and cross correlation. *Geophys. Res. Lett.* 43, 6234–6242. <https://doi.org/10.1002/2016GL069564>.
- Sylvander, M., Souriau, A., 1996. P-velocity structure of the core-mantle boundary region inferred from PKP(AB)-PKP(BC) differential travel times. *Geophys. Res. Lett.* 23, 853–856.
- Tanaka, S., Hamaguchi, H., 1997. Degree one heterogeneity and hemispherical variation of anisotropy in the inner core from PKP(BC)-PKP(DF) times. *J. Geophys. Res.* 102, 2925–2938. <https://doi.org/10.1029/96JB03187>.
- Tauzin, B., Pham, T.-S., Tkalcic, H., 2019. Receiver functions from seismic interferometry: a practical guide. *Geophys. J. Int.* 217, 1–24. <https://doi.org/10.1093/gji/ggz002>.
- Tkalcic, H., 2015. Complex inner core of the Earth: the last frontier of global seismology. *Rev. Geophys.* 53, 59–94. <https://doi.org/10.1002/2014RG000469>.
- Tkalcic, H., 2017. The Earth's Inner Core: Revealed by Observational Seismology. Cambridge University Press. <https://doi.org/10.1017/9781139583954>.
- Tkalcic, H., Pham, T.-S., 2018. Shear properties of Earth's inner core constrained by a detection of J waves in global correlation wavefield. *Science* 362, 329. <https://doi.org/10.1126/science.aau7649>.
- Tkalcic, H., Pham, T.-S., 2020. Excitation of the Global Correlation Wavefield by Large Earthquakes. (Submitted).
- Tkalcic, H., Pham, T.-S., 2002. Constraints on D structure using PKP(AB-DF), PKP(BC-DF) and Pcp-P traveltimes data from broad-band records. *Geophys. J. Int.* 148, 599–616.
- van Driel, M., Nissen-Meyer, T., 2014a. Optimized viscoelastic wave propagation for weakly dissipative media. *Geophys. J. Int.* 199, 1078–1093. <https://doi.org/10.1093/gji/ggu314>.
- van Driel, M., Nissen-Meyer, T., 2014b. Seismic wave propagation in fully anisotropic axisymmetric media. *Geophys. J. Int.* 199, 880–893. <https://doi.org/10.1093/gji/ggu269>.
- van Driel, M., Nissen-Meyer, T., 2015. Instaseis: instant global seismograms based on a broadband waveform database. *Solid Earth* 6, 701–717. <https://doi.org/10.5194/se-6-701-2015>.

- Ventosa, S., Schimmel, M., Stutzmann, E., 2019. Towards the processing of large data volumes with phase cross-correlation. *Seismol. Res. Lett.* 90, 1663–1669. <https://doi.org/10.1785/0220190022>.
- Wang, T., Song, X., 2018. Support for equatorial anisotropy of Earth's inner-inner core from seismic interferometry at low latitudes. *Phys. Earth Planet. Inter.* 276, 247–257. <https://doi.org/10.1016/j.pepi.2017.03.004>. Special Issue: 15th SEDI conference.
- Wang, S., Tkalčić, H., 2020a. Seismic event coda-correlation: toward global coda-correlation tomography. *J. Geophys. Res. Solid Earth* 125<https://doi.org/10.1029/2019JB018848>. e2019JB018848.
- Wang, S., Tkalčić, H., 2020b. Seismic event Coda-Correlation's formation: implications for global seismology. *Geophys. J. Int.* 222, 1283–1294. <https://doi.org/10.1093/gji/ggaa259>.
- Wang, T., Song, X., Xia, H.H., 2015. Equatorial anisotropy in the inner part of Earth's inner core from autocorrelation of earthquake coda. *Nat. Geosci.* 8, 224–227.
- Wapenaar, K., 2004. Retrieving the elastodynamic green's function of an arbitrary inhomogeneous medium by cross correlation. *Phys. Rev. Lett.* 93, 1–4. <https://doi.org/10.1103/physrevlett.93.254301>.
- Wapenaar, K., Fokkema, J., 2006. Green's function representations for seismic interferometry. *Geophysics* 71, SI33–SI46. <https://doi.org/10.1190/1.2213955>.
- Wapenaar, K., Draganov, D., Snieder, R., Campman, X., Verdel, A., 2010. Tutorial on seismic interferometry: Part 1 — Basic principles and applications. *Geophysics* 75, 75A195–75A209. <https://doi.org/10.1190/1.3457445>.
- Waszek, L., Deuss, A., 2011. Distinct layering in the hemispherical seismic velocity structure of Earth's upper inner core. *J. Geophys. Res.* 116, B12313.
- Weaver, R.L., Lobkis, O.I., 2001. Ultrasonics without a source: thermal fluctuation correlations at MHz frequencies. *Phys. Rev. Lett.* 87, 134301. <https://doi.org/10.1103/PhysRevLett.87.134301>.
- Weaver, R.L., Lobkis, O.I., 2004. Diffuse fields in open systems and the emergence of the Green's function (L). *J. Acoust. Soc. Am.* 116, 2731–2734. <https://doi.org/10.1121/1.1810232>.
- Weaver, R.L., Lobkis, O.I., 2006. Diffuse fields in ultrasonics and seismology. *Geophysics* 71. <https://doi.org/10.1190/1.2212247>.
- Wen, L., Niu, F., 2002. Seismic velocity and attenuation structures in the top of the Earth's inner core. *J. Geophys. Res. Solid Earth* 107, 2273. <https://doi.org/10.1029/2001JB000170>.
- Wu, B., Xia, H.H., Wang, T., Shi, X., 2018. Simulation of core phases from coda interferometry. *J. Geophys. Res. Solid Earth* 123, 4983–4999. <https://doi.org/10.1029/2017JB015405>.
- Xia, H.H., Song, X., Wang, T., 2016. Extraction of triplicated PKP phases from noise correlations. *Geophys. J. Int.* 205, 499–508. <https://doi.org/10.1093/gji/ggw015>.
- Yang, Y., Ritzwoller, M.H., Levshin, A.L., Shapiro, N.M., 2007. Ambient noise Rayleigh wave tomography across Europe. *Geophys. J. Int.* 168, 259–274.
- Yao, H., van der Hilst, R.D., de Hoop, M.V., 2006. Surface-wave array tomography in SE Tibet from ambient seismic noise and two-station analysis – I. Phase velocity maps. *Geophys. J. Int.* 166, 732–744. <https://doi.org/10.1111/j.1365-246X.2006.03028.x>.
- Yates, A.S., Savage, M.K., Jolly, A.D., Caudron, C., Hamling, I.J., 2019. Volcanic, coseismic, and seasonal changes detected at White Island (Whakaari) Volcano, New Zealand, using seismic ambient noise. *Geophys. Res. Lett.* 46, 99–108. <https://doi.org/10.1029/2018GL080580>.
- Zhan, Z., Ni, S., Helmberger, D.V., Clayton, R.W., 2010. Retrieval of Moho-reflected shear wave arrivals from ambient seismic noise. *Geophys. J. Int.* 182, 408–420. <https://doi.org/10.1111/j.1365-246X.2010.04625.x>.
- Zheng, S., Sun, X., Song, X., Yang, Y., Ritzwoller, M.H., 2008. Surface wave tomography of China from ambient seismic noise correlation. *Geochem. Geophys. Geosyst.* 9, 1–8. <https://doi.org/10.1029/2008GC001981>.